



UNIVERSIDADE ESTADUAL DE CAMPINAS
SISTEMA DE BIBLIOTECAS DA UNICAMP
REPOSITÓRIO DA PRODUÇÃO CIENTÍFICA E INTELLECTUAL DA UNICAMP

Versão do arquivo anexado / Version of attached file:

Versão do Editor / Published Version

Mais informações no site da editora / Further information on publisher's website:

<https://onlinelibrary.wiley.com/doi/full/10.1002/nme.5308>

DOI: 10.1002/nme.5308

Direitos autorais / Publisher's copyright statement:

©2016 by John Wiley & Sons. All rights reserved.

DIRETORIA DE TRATAMENTO DA INFORMAÇÃO

Cidade Universitária Zeferino Vaz Barão Geraldo

CEP 13083-970 – Campinas SP

Fone: (19) 3521-6493

<http://www.repositorio.unicamp.br>

Hierarchical high-order conforming C^1 bases for quadrangular and triangular finite elements

Luan J. F. Ferreira and Marco L. Bittencourt^{*,†}

Department of Integrated Systems, School of Mechanical Engineering, University of Campinas, Rua Mendeleev 200, Campinas, São Paulo 13083-970, Brazil

SUMMARY

We present three new sets of C^1 hierarchical high-order tensor-product bases for conforming finite elements. The first basis is a high-order extension of the Bogner–Fox–Schmit basis. The edge and face functions are constructed using a combination of cubic Hermite and Jacobi polynomials with C^1 global continuity on the common edges of elements. The second basis uses the tensor product of fifth-order Hermite polynomials and high-order functions and achieves global C^1 continuity for meshes of quadrilaterals and C^2 continuity on the element vertices. The third basis for triangles is also constructed using the tensor product of one-dimensional functions defined in barycentric coordinates. It also has global C^1 continuity on edges and C^2 continuity on vertices. A patch test is applied to the three considered elements. Projection and plate problems with smooth fabricated solutions are solved, and the performance of the h - and p -refinements are evaluated by comparing the approximation errors in the L_2 - and energy norms. A plate with singularity is then studied, and h - and p -refinements are analysed. Finally, a transient problem with implicit time integration is considered. The results show exponential convergence rates with increasing polynomial order for the triangular and quadrilateral meshes of non-distorted and distorted elements. Copyright © 2016 John Wiley & Sons, Ltd.

Received 13 November 2015; Revised 28 April 2016; Accepted 25 May 2016

KEY WORDS: C^1 continuous bases; tensor product bases; high-order finite elements; p - and hp -refinements; Kirchhoff plate

1. INTRODUCTION

The h -version of the finite element method is the most used numerical technique for the analysis of structural problems [1]. In the h -version, solution convergence is achieved by decreasing the element size, while the order of the interpolation functions is fixed. In the p -version, the element size is fixed, and the polynomial order is increased [1–4]. We can combine both versions to obtain the hp -version that refines the mesh and increases the polynomial order. The definition of tensor product polynomial bases is an important aspect of the hp high-order methods in order to achieve good numerical conditioning of the element and global matrices [2, 3]. Most of the proposed bases have C^0 continuity on the element boundary [2, 5]. However, some problems including the Euler–Bernoulli beam, Kirchhoff plate, shells, Stoke’s flow and Cahn–Hilliard equation may require C^1 continuity on the element boundaries to obtain conforming approximate solutions. The construction and implementation of C^1 continuous bases are more difficult. Most of the available C^1 bases for the finite element method uses Hermite polynomials for their construction. Others possibilities are based on Bernstein–Bezier splines [6].

Several C^1 conforming elements for h -version can be found in the literature [7–9]. The most well known are the Argyris triangle, also termed TUBA element [10], and the Bogner–Fox–Schmit (BFS)

^{*}Correspondence to: Marco L. Bittencourt, Department of Integrated Systems, School of Mechanical Engineering, University of Campinas, Rua Mendeleev 200, Campinas, São Paulo 13083-970, Brazil.

[†]E-mail: mlb@fem.unicamp.br

square element [11, 12], both applied to the Kirchhoff plate model. The Argyris triangle uses a fifth-order polynomial approximation and has displacement and first and second partial derivatives as the degrees of freedom on vertices and normal derivatives on edges. This element has a satisfactory accuracy for the h -version, due to the use of fifth-order polynomial approximation. However, the degrees of freedom on edges makes the implementation difficult when compared with the standard finite elements. A modification of the Argyris triangular element that eliminates nodes for the normal derivatives on edges was proposed by Bell [13]. However, this elimination reduced the order of the convergence rate. Okabe [10] derived explicit interpolation formulae for the Argyris triangle, which simplified the implementation of the TUBA element. Recently, Dominguez *et al.* [14] proposed a new algorithm to evaluate the basis functions of the Argyris finite element and their derivatives. The main advantage is an efficient way to calculate the transformation matrix between the Argyris element and the reference system, which makes the implementation simpler. Peano [15] obtained expressions in area coordinates for C^0 and C^1 hierarchical interpolation functions of order P for triangular elements and discussed the requirements to satisfying C^0 and C^1 continuity on element boundaries. However, the implementation of the basis for any order P is difficult because of the interdependency of the functions.

The BFS element is a C^1 conforming square element defined by complete bi-cubic polynomials. It is simple to implement as the interpolation functions can be obtained from the tensor product of cubic Hermite polynomials, and it has expected convergence rates with mesh refinement [8]. However, this element does not have similar convergence rates for distorted meshes [11]. Bernadou [16] proposed a procedure to curve the edges of C^1 triangles, which is compatible with Argyris and Bell elements. Pretera *et al.* [17] described a similar procedure to curve edges of the BFS element. They observed improvement in the solution accuracy when using isoparametric mapping.

High-order polynomial approximation is an alternative to improve the performance and overcome some difficulties of the h -version when applied to structural problems. Wang *et al.* [1] proposed a p -version hierarchical triangular element for plate bending using corrective rational functions. The high-order functions are given by recursive equations in terms of the edge and face functions for each polynomial order. The convergence rate of the p -refinement was twice as high as the h -refinement rate for the same number of degrees of freedom. Šolín *et al.* [18] proposed high-order triangular elements using Lobatto polynomials. Similarly, Scapolla *et al.* [4] developed a new family of C^1 triangular finite elements for plate bending with orders 4, 5 and 6. The starting point was the Bell triangle, and the high-order elements are hierarchical extensions. Each new edge function is zero on the element boundary, and their normal derivatives are non-zero on the edge associated with the function. The face functions are bubbles, and their normal derivatives vanish on all edges of the triangle. The results showed a fast convergence rate for displacement. Papanicolopoulos *et al.* [19] derived a generic formulae for TUBA elements with order greater than 5. They also presented an element with order 7 and third-order derivatives on vertices. The results of benchmark problems in elasticity showed exponential convergence. Walkington [20] presented a tetrahedral C^1 element as an extension of triangular C^1 elements.

Improvements were also proposed for the BFS element. Gopalacharyulu [21] considered second-order derivatives of the primary variable as degrees of freedom on vertices with fourth-order polynomial approximation. Bardell [22] proposed a hierarchical p -refinement, where the approximation order is increased by adding orthogonal shape functions. Recently, Zhang [23], based on the work of Gopalacharyulu [21], presented the construction of rectangles and cuboid elements using P_k -spaces. They showed complete conforming C^1 continuity for this space, and the results exhibited good convergence rate. Ahmadi *et al.* [24] observed that the discontinuities in the first-order derivatives of dependent variables in space and time introduced perturbations on the solution and eventually led to failure of time discrete schemes. They used the BFS element to solve the problem marching in space and time. In another work, Surana *et al.* [25] proposed C^k Hermite finite elements, and the results showed that increasing the continuity improves the convergence rate, but little improvement was observed for $k > 2$.

We propose the construction of C^1 high-order shape functions for triangular and square conforming elements using the tensor product of one-dimensional polynomial bases. The high-order hierarchical functions are built using third- and fifth-order Hermite polynomials. Because of their

tensorial feature, the proposed bases are simpler to construct when compared with the other bases available in the literature and may have an arbitrary polynomial order. In addition, meshes of quadrilateral elements may be used. The performance of the high-order elements is evaluated using a patch test, projection and two-plate problems solved by h - and p -refinements. Results for a plate with singularity and an implicit transient analysis are also presented. The equivalence between the projection and plate problems is considered, and the convergence rates are compared with the estimated theoretical rates. The developed bases can be applied to any problem, which requires C^1 continuity, and we consider here the approximation of the Kirchhoff plate. This paper is organized in the following six sections. First, a brief review about the Kirchhoff plate model is presented. In Sections 3–5, we develop the high-order interpolation functions for squares and triangles. Section 6 considers the numerical results, and finally, the conclusions are addressed.

2. APPROXIMATION OF THE KIRCHHOFF PLATE

The differential equation of equilibrium for the Kirchhoff plate model is given by [3]

$$\frac{\partial^2}{\partial x^2} \left[-D \left(\frac{\partial^2 w}{\partial x^2} + \nu \frac{\partial^2 w}{\partial y^2} \right) \right] + 2 \frac{\partial^2}{\partial x \partial y} \left[-D(1-\nu) \frac{\partial^2 w}{\partial x \partial y} \right] + \frac{\partial^2}{\partial y^2} \left[-D \left(\frac{\partial^2 w}{\partial y^2} + \nu \frac{\partial^2 w}{\partial x^2} \right) \right] + q = 0 \tag{2.1}$$

Assuming constant material and geometric properties, we obtain

$$D \left(\frac{\partial^4 w}{\partial x^4} + 2 \frac{\partial^4 w}{\partial x^2 \partial y^2} + \frac{\partial^4 w}{\partial y^4} \right) - q = 0 \tag{2.2}$$

where $D = \frac{Et^3}{12(1-\nu^2)}$, $w = w(x, y)$ is the transversal displacement of the middle surface, $q = q(x, y)$ is the transversal distributed loading, E and ν are the Young’s modulus and Poisson’s ratio of the material, respectively, and t is the thickness.

The weak form associated with (2.2) is given by [3]

$$D \int_A \left[\frac{\partial^2 w}{\partial x^2} \frac{\partial^2 v}{\partial x^2} + \frac{\partial^2 w}{\partial y^2} \frac{\partial^2 v}{\partial y^2} + \nu \left(\frac{\partial^2 w}{\partial x^2} \frac{\partial^2 v}{\partial y^2} + \frac{\partial^2 w}{\partial y^2} \frac{\partial^2 v}{\partial x^2} \right) + 2(1-\nu) \frac{\partial^2 w}{\partial x \partial y} \frac{\partial^2 v}{\partial x \partial y} \right] dA + \int_{\Gamma} \left(V_n + \frac{\partial M_{nt}}{\partial t} \right) v d\Gamma - \int_{\Gamma} M_{nn} \frac{\partial v}{\partial n} d\Gamma - \int_A q v dA - \sum_{i=1}^n [(M_{nt}^+ - M_{nt}^-) v]_i + \sum_{j=1}^m P_j v = 0 \tag{2.3}$$

where V_n , M_{nn} and M_{nt} are the shear force, bending moment and twist moment on the boundary of the normal plane, respectively, as shown in Figure 1 and P_j denotes the concentrated loads. Loads in the normal and xy planes are related by

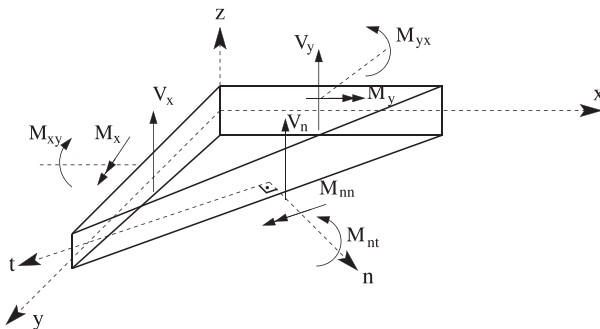


Figure 1. Loads on the plate boundary in planes xy and nt [3].

$$V_n = V_x n_x + V_y n_y$$

$$M_{nn} \frac{\partial v}{\partial n} + M_{nt} \frac{\partial v}{\partial t} = \left(M_{xx} \frac{\partial v}{\partial x} + M_{xy} \frac{\partial v}{\partial y} \right) n_x + \left(M_{xy} \frac{\partial v}{\partial x} + M_{yy} \frac{\partial v}{\partial y} \right) n_y \quad (2.4)$$

The bending and twisting moments are calculated as

$$M_{xx} = -D \left(\frac{\partial^2 w}{\partial x^2} + \nu \frac{\partial^2 w}{\partial y^2} \right) \quad (2.5)$$

$$M_{yy} = -D \left(\frac{\partial^2 w}{\partial y^2} + \nu \frac{\partial^2 w}{\partial x^2} \right) \quad (2.6)$$

$$M_{xy} = -D(1 - \nu) \frac{\partial^2 w}{\partial x \partial y} \quad (2.7)$$

The displacement w can be interpolated in each finite element of a mesh as the following linear combination

$$w = \mathbf{N}_e^T \mathbf{d}_e \quad (2.8)$$

where \mathbf{N}_e is the matrix of shape functions and \mathbf{d}_e represents the vector of unknown coefficients. Using the Galerkin method, the weak form (2.3) of the Kirchhoff plate is interpolated in a mesh of nel elements as

$$\begin{aligned} & \bigcup_{e=1}^{nel} \int_{A_e} \left[\frac{\partial^2 \mathbf{N}_e^T}{\partial x^2} \frac{\partial^2 \mathbf{N}_e}{\partial x^2} + \frac{\partial^2 \mathbf{N}_e^T}{\partial y^2} \frac{\partial^2 \mathbf{N}_e}{\partial y^2} + \nu \left(\frac{\partial^2 \mathbf{N}_e^T}{\partial x^2} \frac{\partial^2 \mathbf{N}_e}{\partial y^2} + \frac{\partial^2 \mathbf{N}_e^T}{\partial y^2} \frac{\partial^2 \mathbf{N}_e}{\partial x^2} \right) \right. \\ & \quad \left. + 2(1 - \nu) \frac{\partial^2 \mathbf{N}_e^T}{\partial x \partial y} \frac{\partial^2 \mathbf{N}_e}{\partial x \partial y} \right] dA_e \mathbf{d}_e \\ & + \int_{\Gamma_e} \mathbf{N}_e^T \left(V_n + \frac{\partial M_{nt}}{\partial t} \right) d\Gamma_e - \int_{\Gamma_e} \frac{\partial \mathbf{N}_e^T}{\partial n} M_{nn} d\Gamma_e - \int_{A_e} \mathbf{N}_e^T q dA_e \\ & - \sum_{i=1}^n [\mathbf{N}_e^T (M_{nt}^+ - M_{nt}^-)]_i + \sum_{j=1}^m \mathbf{N}_e^T P_j = 0 \end{aligned} \quad (2.9)$$

and \bigcup indicates the standard assembly procedure. The aforementioned expression can be rewritten as

$$\bigcup_{e=1}^{nel} \mathbf{K}_e \mathbf{d}_e - \mathbf{f}_e = 0 \quad (2.10)$$

The element stiffness matrix \mathbf{K}_e and load vector \mathbf{f}_e are given, respectively, by

$$\mathbf{K}_e = D \int_{A_e} \left[\frac{\partial^2 \mathbf{N}_e^T}{\partial x^2} \frac{\partial^2 \mathbf{N}_e}{\partial x^2} + \frac{\partial^2 \mathbf{N}_e^T}{\partial y^2} \frac{\partial^2 \mathbf{N}_e}{\partial y^2} + \nu \left(\frac{\partial^2 \mathbf{N}_e^T}{\partial x^2} \frac{\partial^2 \mathbf{N}_e}{\partial y^2} + \frac{\partial^2 \mathbf{N}_e^T}{\partial y^2} \frac{\partial^2 \mathbf{N}_e}{\partial x^2} \right) \right. \\ \left. + 2(1 - \nu) \frac{\partial^2 \mathbf{N}_e^T}{\partial x \partial y} \frac{\partial^2 \mathbf{N}_e}{\partial x \partial y} \right] dA_e \quad (2.11)$$

$$\mathbf{f}_e = \int_{\Gamma_e} \mathbf{N}_e^T \left(V_n + \frac{\partial M_{nt}}{\partial t} \right) d\Gamma_e - \int_{\Gamma_e} \frac{\partial \mathbf{N}_e^T}{\partial n} M_{nn} d\Gamma_e - \int_{A_e} \mathbf{N}_e^T q dA_e \\ - \sum_{i=1}^n [\mathbf{N}_e^T (M_{nt}^+ - M_{nt}^-)]_i + \sum_{j=1}^m \mathbf{N}_e^T P_j = 0 \quad (2.12)$$

The element stiffness matrix can be rewritten in the standard form:

$$\mathbf{K}_e = \frac{t^3}{12} \int_{A_e} \mathbf{B}_e^T \mathbf{D} \mathbf{B}_e dA_e \tag{2.13}$$

and the strain–displacement \mathbf{B}_e and elasticity \mathbf{D} matrices are

$$\mathbf{B}_e = \begin{bmatrix} -\frac{\partial^2 \mathbf{N}_e}{\partial x^2} \\ -\frac{\partial^2 \mathbf{N}_e}{\partial y^2} \\ -2 \frac{\partial^2 \mathbf{N}_e}{\partial x \partial y} \end{bmatrix} \text{ and } \mathbf{D} = \frac{E}{(1-\nu^2)} \begin{bmatrix} 1 & \nu & 0 \\ \nu & 1 & 0 \\ 0 & 0 & \frac{1-\nu}{2} \end{bmatrix} \tag{2.14}$$

The stiffness matrix for the quadrangular element in the standard domain is

$$\mathbf{K}_e = \frac{t^3}{12} \int_{-1}^1 \int_{-1}^1 \mathbf{B}_e^T \mathbf{D} \mathbf{B}_e \det \mathbf{J} d\xi d\eta \tag{2.15}$$

The Jacobian and strain–displacement matrices are given, respectively, as

$$\mathbf{J} = \begin{bmatrix} x, \xi & x, \eta \\ y, \xi & y, \eta \end{bmatrix}, \mathbf{j} = \mathbf{J}^{-1} \tag{2.16}$$

$$\mathbf{B}_e = \mathbf{C} \mathbf{S}_e + \mathbf{T} \bar{\mathbf{B}}_e, \mathbf{C} = -\mathbf{T} \mathbf{C}_1 \mathbf{j} \tag{2.17}$$

$$\mathbf{C}_1 = \begin{bmatrix} J_{11, \xi} & J_{12, \xi} \\ J_{21, \eta} & J_{22, \eta} \\ (J_{11, \eta} + J_{21, \xi}) & (J_{12, \eta} + J_{22, \xi}) \end{bmatrix}, \mathbf{S}_e = \left\{ \begin{matrix} \frac{\partial \mathbf{N}_e(\xi, \eta)}{\partial \xi} \\ \frac{\partial \mathbf{N}_e(\xi, \eta)}{\partial \eta} \end{matrix} \right\} \tag{2.18}$$

$$\mathbf{T} = \begin{bmatrix} j_{11}^2 & j_{12}^2 & 2 j_{11} j_{12} \\ j_{21}^2 & j_{22}^2 & 2 j_{21} j_{22} \\ 2 j_{11} j_{12} & 2 j_{21} j_{22} & 2 (j_{11} j_{22} + j_{12} j_{21}) \end{bmatrix}, \bar{\mathbf{B}}_e = \begin{bmatrix} -\frac{\partial^2 \mathbf{N}_e(\xi, \eta)}{\partial \xi^2} \\ -\frac{\partial^2 \mathbf{N}_e(\xi, \eta)}{\partial \eta^2} \\ -2 \frac{\partial^2 \mathbf{N}_e(\xi, \eta)}{\partial \xi \partial \eta} \end{bmatrix} \tag{2.19}$$

with \mathbf{C} , \mathbf{C}_1 and \mathbf{T} are the matrices that transform second-order derivatives in the standard domain to the physical domain and \mathbf{S}_e and $\bar{\mathbf{B}}_e$ are the local matrices of first-order and second-order derivatives, respectively [11].

3. HIERARCHICAL H_3 HIGH-ORDER SQUARE ELEMENT

The Kirchhoff plate theory leads to the element stiffness matrix in terms of the global second-order derivatives of the shape functions. Therefore, the conforming finite elements for the Kirchhoff plate should provide continuity of the transversal displacement and its first-order partial derivatives. The most known C^1 conforming square element is the four-node BFS element [8]. It is the starting point of the H_3 high-order finite element here presented. The BFS element has 16 degrees of freedom associated with w , $w_{,x}$, $w_{,y}$ and $w_{,xy}$ for each vertex node. The shape functions can be obtained by the tensor product of the one-dimensional cubic Hermite polynomials [8, 11] given in the local coordinate system $\xi \in [-1, 1]$ by

$$\begin{aligned} h_1(\xi) &= \frac{1}{4} (2 - 3\xi + \xi^3) \\ h_2(\xi) &= \frac{1}{4} (1 - \xi - \xi^2 + \xi^3) \\ h_3(\xi) &= \frac{1}{4} (2 + 3\xi - \xi^3) \\ h_4(\xi) &= \frac{1}{4} (1 - \xi + \xi^2 + \xi^3) \end{aligned} \tag{3.1}$$

Figure 2 shows the cubic Hermite polynomials and their first partial derivatives. Because of the collocation property, the polynomials h_1 and h_3 are associated with the interpolated function and h_2 and h_4 with its first-order derivative.

The approximation of the transversal displacement in the standard square is written as

$$w(\xi, \eta) = \sum_{i=a}^d \phi_1^i(\xi, \eta) w^i + \phi_2^i(\xi, \eta) w_{,\xi}^i + \phi_3^i(\xi, \eta) w_{,\eta}^i + \phi_4^i(\xi, \eta) w_{,\xi\eta}^i = \mathbf{N}_e^T \bar{\mathbf{d}}_e \quad (3.2)$$

where the shape functions are given by the tensor product of the one-dimensional cubic Hermite polynomials

$$\phi_j^i(\xi, \eta) = h_p(\xi) h_q(\eta) \quad i = a, b, \dots, d \text{ and } j = 1, 2, \dots, 4 \quad (3.3)$$

with index i related to the degrees of freedom of node j and p and q are the indices of the one-dimensional cubic Hermite polynomials given in (3.1). The vector of unknown local coefficients $\bar{\mathbf{d}}_e$ is written as

$$\bar{\mathbf{d}}_e = \left\{ \bar{\mathbf{d}}_{\xi\eta}^a \quad \bar{\mathbf{d}}_{\xi\eta}^b \quad \bar{\mathbf{d}}_{\xi\eta}^c \quad \bar{\mathbf{d}}_{\xi\eta}^d \right\}^T \text{ and } \bar{\mathbf{d}}_{\xi\eta}^i = \left\{ w^i \quad w_{,\xi}^i \quad w_{,\eta}^i \quad w_{,\xi\eta}^i \right\}^T \quad (3.4)$$

The tensor product procedure is illustrated in Figure 3, and the tensor indices p and q are given in Table I. The indices 1 and 3 are associated with the one-dimensional cubic Hermite polynomials h_1 and h_3 , which represent displacement. Indices 2 and 4 are associated with the one-dimensional functions h_2 and h_4 , which represent slopes. The shape functions $\phi_1^a, \phi_2^a, \phi_3^a$ and ϕ_4^a are associated respectively with degrees of freedom $w^a, w_{,\xi}^a, w_{,\eta}^a$ and $w_{,\xi\eta}^a$ of node a .

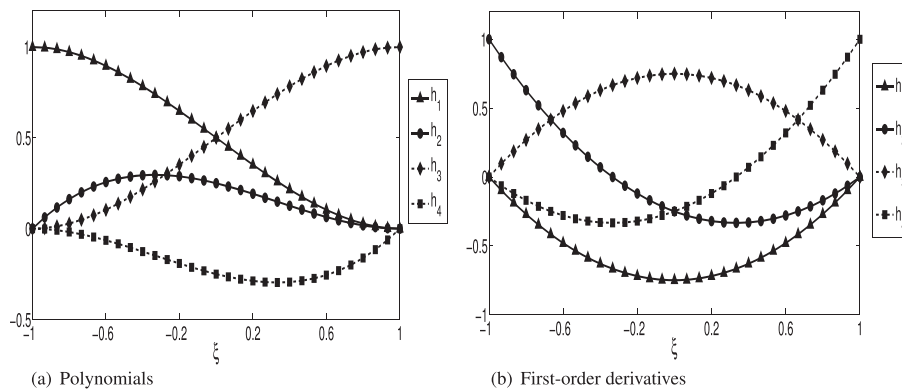


Figure 2. Cubic Hermite polynomials and their first-order derivatives.

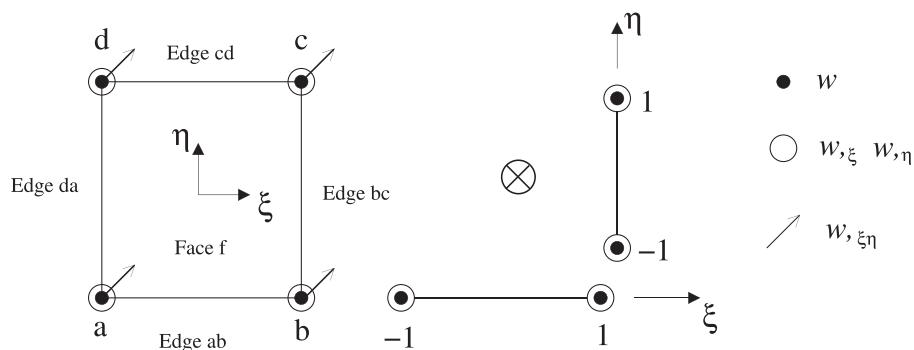


Figure 3. Tensor product of one-dimensional cubic Hermite polynomials for the Bogner–Fox–Schmit element and its degrees of freedom.

The approximation for $w(\xi, \eta)$ in (3.2) is in terms of the standard domain and the local degrees of freedom $w^i, w_{,\xi}^i, w_{,\eta}^i$ and $w_{,\xi\eta}^i$. However, the finite element stiffness matrices are calculated in the physical domain. Therefore, we use the transformation matrix \mathbf{A} that relates the degrees of freedom in the standard and physical domains as $\mathbf{d}_e = \mathbf{A} \bar{\mathbf{d}}_e$ [11] and

$$w(x, y) = \mathbf{N}_e^T(x, y) \mathbf{d}_e = \mathbf{N}_e^T(\xi, \eta) \mathbf{A} \bar{\mathbf{d}}_e \tag{3.5}$$

where

$$\mathbf{d}_e = \begin{Bmatrix} \mathbf{d}_a \\ \mathbf{d}_b \\ \mathbf{d}_c \\ \mathbf{d}_d \end{Bmatrix}, \mathbf{d}_i = \begin{Bmatrix} w^i \\ w_{,x}^i \\ w_{,y}^i \\ w_{,xy}^i \end{Bmatrix}, \bar{\mathbf{d}}_e = \begin{Bmatrix} \bar{\mathbf{d}}_a \\ \bar{\mathbf{d}}_b \\ \bar{\mathbf{d}}_c \\ \bar{\mathbf{d}}_d \end{Bmatrix}, \bar{\mathbf{d}}_i = \begin{Bmatrix} w^i \\ w_{,\xi}^i \\ w_{,\eta}^i \\ w_{,\xi\eta}^i \end{Bmatrix} \tag{3.6}$$

$$\mathbf{A} = \begin{bmatrix} \bar{\mathbf{A}} & \mathbf{0} & \mathbf{0} & \mathbf{0} \\ \mathbf{0} & \bar{\mathbf{A}} & \mathbf{0} & \mathbf{0} \\ \mathbf{0} & \mathbf{0} & \bar{\mathbf{A}} & \mathbf{0} \\ \mathbf{0} & \mathbf{0} & \mathbf{0} & \bar{\mathbf{A}} \end{bmatrix}, \bar{\mathbf{A}} = \begin{bmatrix} 1 & 0 & 0 & 0 \\ 0 & j_{11} & j_{12} & 0 \\ 0 & j_{21} & j_{22} & 0 \\ 0 & 0 & 0 & j_{11}j_{22} + j_{12}j_{21} \end{bmatrix} \tag{3.7}$$

The hierarchical H_3 high-order element starts from the BFS element, and new edge and face functions are added for $P \geq 4$. These high-order functions do not change the properties of the vertex functions and improve the solution accuracy on the element. The one-dimensional high-order functions used in the tensor product given in (3.3) are [3]

$$h_{P+1}(\xi) = \frac{\partial h_1(\xi)}{\partial \xi} (1 - \xi^2) J_{P-4}^{1,1}(\xi), \quad P \geq 4 \tag{3.8}$$

where $J_{P-4}^{1,1}(\xi)$ denotes the Jacobi polynomials of order $P - 4$ with weights $(1, 1)$. These functions of order P together with the cubic Hermite polynomials compose a hierarchical basis. Figure 4 shows the high-order one-dimensional functions and their first derivatives for $P = 7$. They are zero on the element boundaries.

The H_3 square high-order functions can be obtained from the standard tensor product. Two shape functions exist for each edge of the element and polynomial order corresponding to the transversal displacement and rotation in the normal direction. Thus, the element has $8(P - 3)$ edge functions. The number of face functions for any order P is $(P - 3)^2$, and they related to the transversal

Table I. Indices p and q for the shape functions of the Bogner–Fox–Schmit element.

| ϕ | ϕ_1^a | ϕ_2^a | ϕ_3^a | ϕ_4^a | ϕ_1^b | ϕ_2^b | ϕ_3^b | ϕ_4^b | ϕ_1^c | ϕ_2^c | ϕ_3^c | ϕ_4^c | ϕ_1^d | ϕ_2^d | ϕ_3^d | ϕ_4^d |
|--------|------------|------------|------------|------------|------------|------------|------------|------------|------------|------------|------------|------------|------------|------------|------------|------------|
| p | 1 | 1 | 2 | 2 | 3 | 3 | 4 | 4 | 3 | 3 | 4 | 4 | 1 | 1 | 2 | 2 |
| q | 1 | 2 | 1 | 2 | 1 | 2 | 1 | 2 | 3 | 4 | 3 | 4 | 3 | 4 | 3 | 4 |

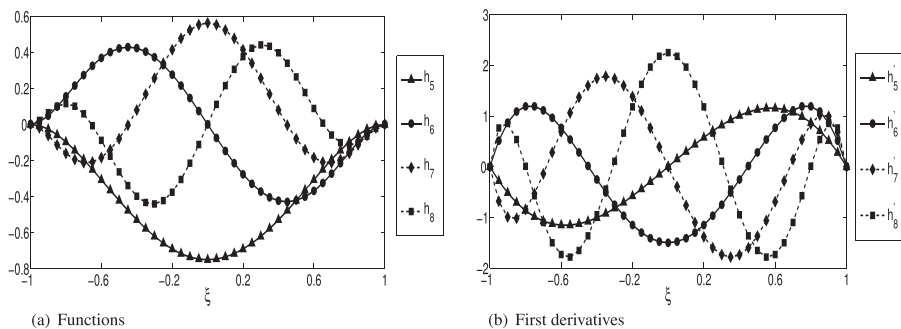


Figure 4. High-order one-dimensional shape functions used in the H_3 element for $P = 7$.

displacement. There are 16 vertex shape functions for $P = 3$. For $P = 4$, there are 16 vertex functions, 8 edge functions and 1 face function with a total of 25 shape functions.

The interpolation of w in the standard domain can be written as

$$w(\xi, \eta) = \underbrace{\sum_{i=1}^{16} a_i \phi_i(\xi, \eta)}_{\text{vertices}} + \underbrace{\sum_{j=1}^{8(P-3)} b_j \phi_j(\xi, \eta)}_{\text{edges}} + \underbrace{\sum_{k=1}^{(P-3)^2} c_k \phi_k(\xi, \eta)}_{\text{faces}} \quad (3.9)$$

with

$$\phi_i(\xi, \eta) = h_p(\xi) h_q(\eta) \quad (3.10)$$

Figure 5 shows the functions ϕ_1^{ab} , ϕ_2^{ab} and ϕ_1^f for $P = 4$. The first edge function ϕ_1^{ab} is related to the displacement degree of freedom, whereas the second edge function ϕ_2^{ab} related to the rotation degree of freedom is zero on the element boundary.

The tensor indices p and q are calculated for $P \geq 4$ as

- edge ab : $p = P + 1, q = 1, 2$;
- edge bc : $p = 3, 4, q = P + 1$;
- edge cd : $p = P + 1, q = 4, 3$;
- edge da : $p = 2, 1, q = P + 1$; and
- face f : $p, q \geq P$ and $p + q \leq 2P + 2$.

The tensor indices p and q for the edge and face functions are given in Table II for $P = 5$.

The H_3 high-order element has exponential convergence rates for meshes of non-distorted elements as presented in Section 6. However, the convergence rates deteriorate for distorted elements because of the loss of C^1 continuity on the common edges of the elements. The H_5 high-order element presented in the next section does not have this limitation.

4. HIERARCHICAL H_5 HIGH-ORDER SQUARE ELEMENT

The one-dimensional C^2 fifth-order Hermite polynomials are given by [11]

$$\begin{aligned} H_1(\xi) &= \frac{1}{16} (1 - \xi)^3 (8 + 9\xi + 3\xi^2) & H_4(\xi) &= \frac{1}{16} (1 + \xi)^3 (8 - 9\xi + 3\xi^2) \\ H_2(\xi) &= \frac{1}{16} (1 - \xi)^3 (1 + \xi) (5 + 3\xi) & H_5(\xi) &= \frac{1}{16} (1 + \xi)^3 (\xi - 1) (5 - 3\xi) \\ H_3(\xi) &= \frac{1}{16} (1 - \xi)^3 (1 + \xi)^2 & H_6(\xi) &= \frac{1}{16} (1 + \xi)^3 (1 - \xi)^2 \end{aligned} \quad (4.1)$$

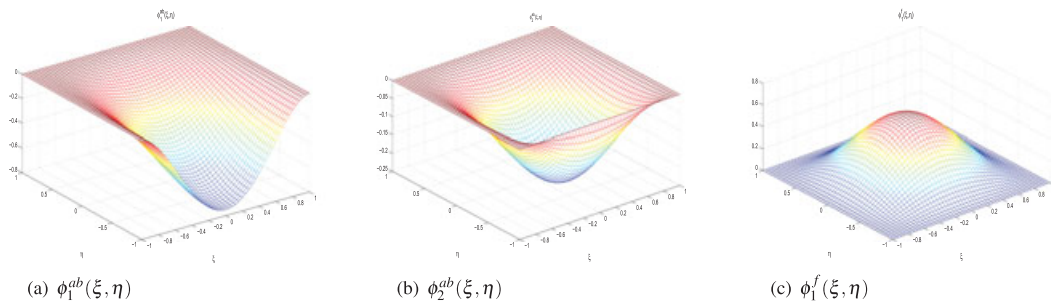


Figure 5. Shape functions for edge ab and face for the hierarchical H_3 high-order finite element and $P = 4$.

Table II. Tensor indices for the H_3 high-order element for $P = 5$.

| ϕ | ϕ_3^{ab} | ϕ_4^{ab} | ϕ_3^{bc} | ϕ_4^{bc} | ϕ_4^{cd} | ϕ_3^{cd} | ϕ_4^{da} | ϕ_3^{da} | ϕ_2^f | ϕ_3^f | ϕ_4^f |
|--------|---------------|---------------|---------------|---------------|---------------|---------------|---------------|---------------|------------|------------|------------|
| p | 6 | 6 | 3 | 4 | 6 | 6 | 2 | 1 | 5 | 6 | 6 |
| q | 1 | 2 | 6 | 6 | 4 | 3 | 6 | 6 | 6 | 5 | 6 |

Figure 6 shows these polynomials and their first- and second-order derivatives. They are used to construct the vertex shape functions of the H_5 quadrilateral element using tensor product. They also have collocation properties similar to the cubic Hermite polynomials.

The fifth-order square element has 24 vertex functions with 6 degrees of freedom per node related to $w, w_x, w_y, w_{xx}, w_{yy}$ and w_{xy} ; 4 edge functions for the normal derivative w_n ; and 1 face function associated with w . The tensor product indices p and q of Equation (3.3) for the vertex shape functions are given in Table III. Indices 1 and 4 are associated with functions that represent displacements of the one-dimensional fifth-order Hermite polynomials, indices 2 and 5 are associated with functions for the first derivative of displacement and indices 3 and 6 are associated with functions that represent second derivatives of displacement.

We construct the edge and face functions using the tensor product of the fifth-order Hermite polynomials and the following high-order one-dimensional functions:

$$H_{P+2}(\xi) = (1 - \xi^2) \frac{dH_1(\xi)}{d\xi} J_{P-5}^{1,1}(\xi) P \geq 5 \tag{4.2}$$

Figure 7 shows these functions and their first- and second-order derivatives for polynomial orders from $P = 5$ to $P = 8$. They are zero on the element boundaries. The tensor indices for edge and

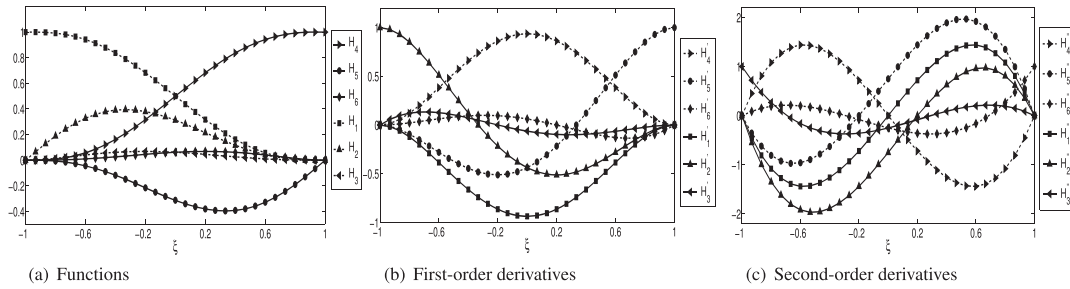


Figure 6. One-dimensional fifth-order Hermite polynomials and their derivatives.

Table III. Tensor indices p and q for the vertex shape functions of the H_5 square element.

| ϕ | ϕ_1^a | ϕ_2^a | ϕ_3^a | ϕ_4^a | ϕ_5^a | ϕ_6^a | ϕ_1^b | ϕ_2^b | ϕ_3^b | ϕ_4^b | ϕ_5^b | ϕ_6^b |
|--------|------------|------------|------------|------------|------------|------------|------------|------------|------------|------------|------------|------------|
| p | 1 | 2 | 1 | 3 | 1 | 2 | 4 | 5 | 4 | 6 | 4 | 5 |
| q | 1 | 1 | 2 | 1 | 3 | 2 | 1 | 1 | 2 | 1 | 3 | 2 |
| ϕ | ϕ_1^c | ϕ_2^c | ϕ_3^c | ϕ_4^c | ϕ_5^c | ϕ_6^c | ϕ_1^d | ϕ_2^d | ϕ_3^d | ϕ_4^d | ϕ_5^d | ϕ_6^d |
| p | 4 | 5 | 4 | 6 | 4 | 5 | 1 | 2 | 1 | 3 | 1 | 2 |
| q | 4 | 4 | 5 | 4 | 6 | 5 | 4 | 4 | 5 | 4 | 6 | 5 |

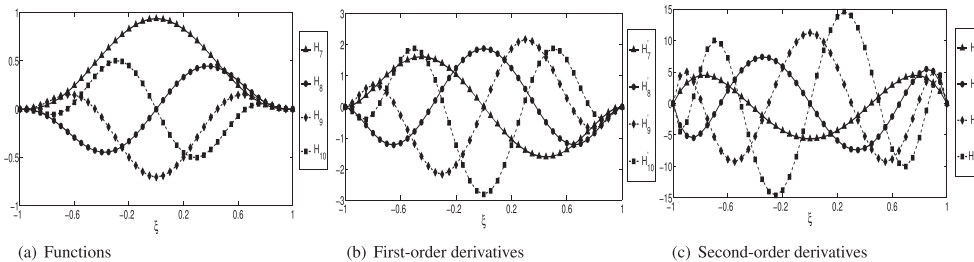


Figure 7. High-order C^2 one-dimensional polynomials and their first- and second-order derivatives from $P = 5$ to $P = 8$.

face shape functions for $P = 5$ and $P = 6$ are given in Table IV. The number of edge and face functions for each order $P \geq 5$ is $4(2P - 9)$ and $(P - 4)^2$, respectively.

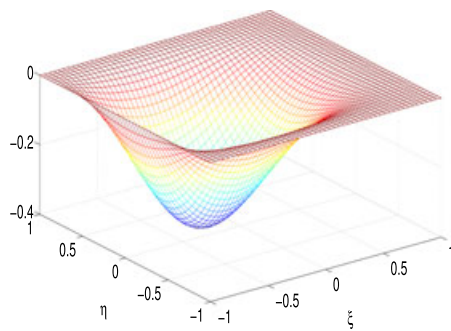
Tensor indices p and q are calculated for $P \geq 5$ using

- edge ab : for $P = 5$, $p = P + 2$ and $q = 2$; for $P > 5$, $p = P + 2$ and $q = 2, 1$;
- edge bc : for $P = 5$, $p = 5$ and $q = P + 2$; for $P > 5$, $p = 5, 4$ and $q = P + 2$;
- edge cd : for $P = 5$, $p = P + 1$ and $q = 5$; for $P > 5$, $p = P + 2$ and $q = 4, 5$;
- edge da : for $P = 5$, $p = 2$ and $q = P + 2$; for $P > 5$, $p = 1, 2$ and $q = P + 2$; and
- face f : $p, q \geq P$ and $p + q \leq 2P + 2$.

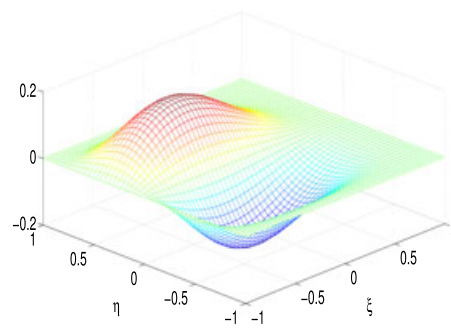
Figure 8 shows the edge function ϕ_1^{ab} and face function ϕ_1^f for $P = 5$ and edge functions ϕ_2^{ab} and ϕ_3^{ab} for $P = 6$. For $P = 5$, there is only one shape function for each edge to be compatible with the high-order triangular element to be presented in the next section. High-order edge functions

Table IV. Tensor indices p and q for the edge and face functions of the H_5 square element for $P = 5$ and $P = 6$.

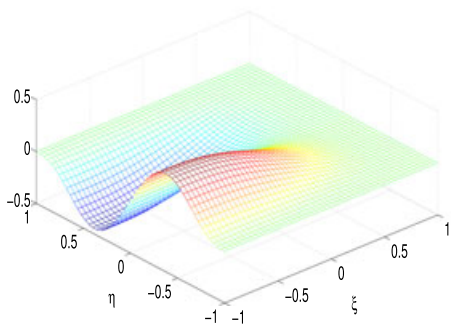
| [P = 5] | | | | | | | | | | | |
|---------|---------------|---------------|---------------|---------------|---------------|---------------|---------------|---------------|------------|------------|------------|
| | ϕ | ϕ_1^{ab} | ϕ_1^{bc} | ϕ_1^{cd} | ϕ_1^{da} | ϕ_1^f | | | | | |
| | p | 7 | 5 | 7 | 2 | 7 | | | | | |
| | q | 2 | 7 | 5 | 7 | 7 | | | | | |
| [P = 6] | | | | | | | | | | | |
| ϕ | ϕ_2^{ab} | ϕ_3^{ab} | ϕ_2^{bc} | ϕ_3^{bc} | ϕ_2^{cd} | ϕ_3^{cd} | ϕ_2^{da} | ϕ_3^{da} | ϕ_2^f | ϕ_3^f | ϕ_4^f |
| p | 8 | 8 | 5 | 4 | 8 | 8 | 1 | 2 | 8 | 7 | 8 |
| q | 2 | 1 | 8 | 8 | 4 | 5 | 8 | 8 | 7 | 8 | 8 |



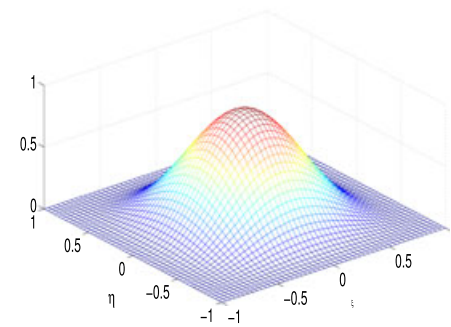
(a) ϕ_1^{ab} , $P = 5$, associated with $w_{,n}$



(b) ϕ_2^{ab} , $P = 6$, associated with $w_{,n}$



(c) ϕ_3^{ab} , $P = 6$, associated with w



(d) ϕ_1^f , $P = 5$, associated with w

Figure 8. Edge and face shape functions for the H_5 high-order square element.

associated with w appear from $P \geq 6$. The first- and second-order derivatives of the second edge shape function associated with w are zero on the element boundary.

Figure 9 shows the continuity of the first edge shape function for $P = 6$, and its first- and second-order partial derivatives in x , y and in the normal direction n on the common edge of the elements are illustrated in Figure 9. The normal derivatives are given by

$$\phi_{1,n}^{ab} = n_x \phi_{1,x}^{ab} + n_y \phi_{1,y}^{ab}, \tag{4.3}$$

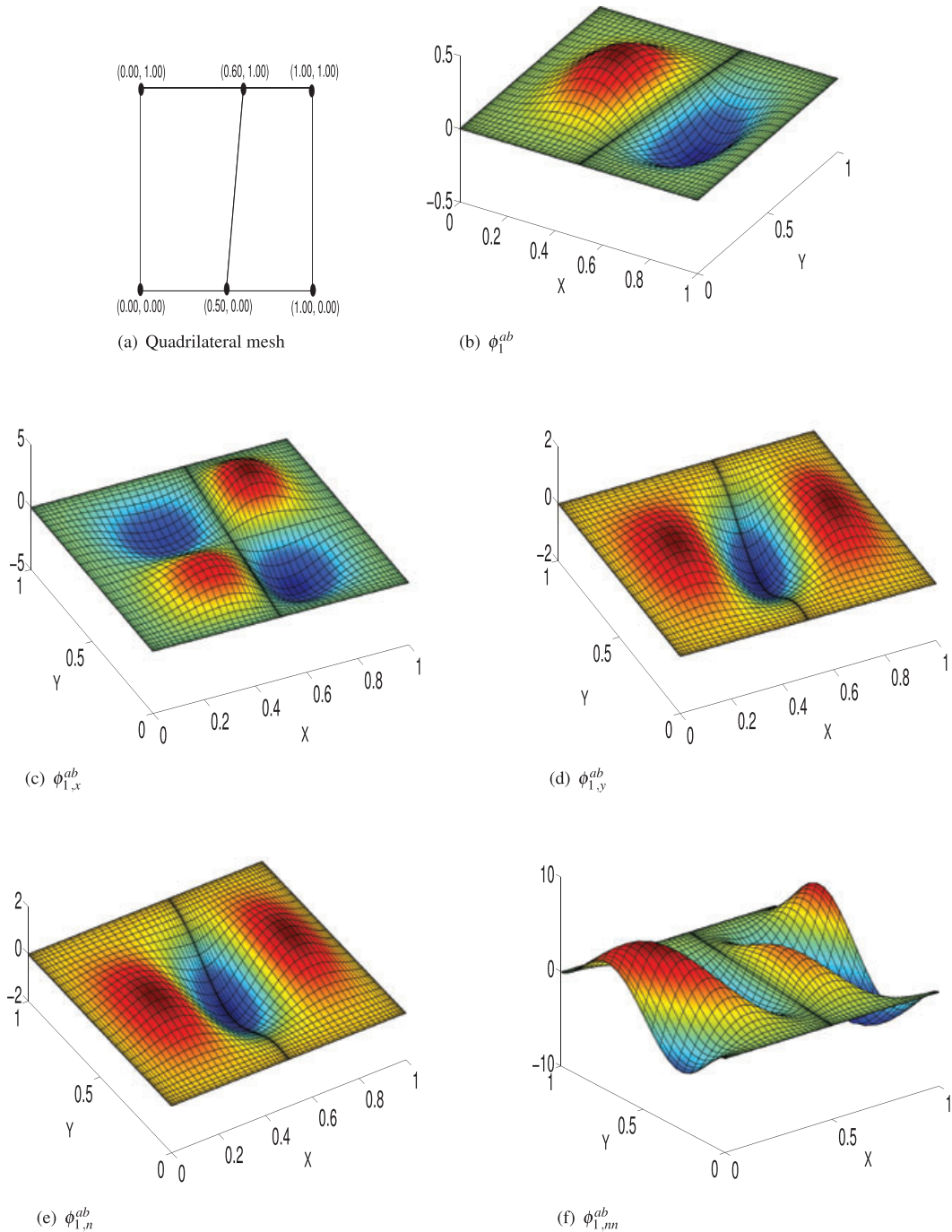


Figure 9. Continuity of the first edge shape function and its first- and second-order partial derivatives on the common edge of two elements for $P = 6$.

$$\phi_{1,nn}^{ab} = n_x^2 \phi_{1,xx}^{ab} + 2n_x n_y \phi_{1,xy}^{ab} + n_y^2 \phi_{1,yy}^{ab} \tag{4.4}$$

where (n_x, n_y) are the components of the normal vector to the edge. The normal vector \mathbf{n} is computed from

$$\mathbf{n} = \mathbf{t}_{ij} \times \mathbf{e}_3 \tag{4.5}$$

where \mathbf{e}_3 is the unit normal vector to the plane defined by the element and \mathbf{t}_{ij} is the tangential vector on edge ij . The edges of the square and triangular elements are shown in Figures 3 and 11, respectively. The components of the tangential vector are

$$\mathbf{t} = \{x_j - x_i, y_j - y_i, 0\}^T \tag{4.6}$$

where (x_i, y_i) and (x_j, y_j) are the coordinates of nodes i and j of edge ij .

According to the Pascal triangle, a C^1 conforming four-node square element requires 4 degrees of freedom per node as in the H_3 element. The C^2 square element requires 9 degrees of freedom per node [3, 11]. The H_5 element has 6 degrees of freedom per node, one for each edge and face and C^2 continuity is also achieved in the vertex nodes.

The approximation for the transversal displacement $w(\xi, \eta)$ in the standard element has the degrees of freedom $w^i, w_{,\xi}^i, w_{,\eta}^i, w_{,\xi\xi}^i, w_{,\eta\eta}^i$ and $w_{,\xi\eta}^i$ for each node. However, the stiffness matrix requires the global derivatives of the shape functions. We can use matrix \mathbf{A} to map the standard to the global degrees of freedom as [11]

$$w(x, y) = \mathbf{N}_e^T(\xi, \eta) \mathbf{d}_e = \mathbf{N}_e^T(\xi, \eta) \mathbf{A} \bar{\mathbf{d}}_e \tag{4.7}$$

where

$$\mathbf{d}_e = \begin{Bmatrix} \mathbf{d}_a \\ \mathbf{d}_b \\ \mathbf{d}_c \\ \mathbf{d}_d \end{Bmatrix}, \mathbf{d}_i = \begin{Bmatrix} w^i \\ w_{,x}^i \\ w_{,y}^i \\ w_{,xx}^i \\ w_{,yy}^i \\ w_{,xy}^i \end{Bmatrix}, \bar{\mathbf{d}}_e = \begin{Bmatrix} \bar{\mathbf{d}}_a \\ \bar{\mathbf{d}}_b \\ \bar{\mathbf{d}}_c \\ \bar{\mathbf{d}}_d \end{Bmatrix}, \bar{\mathbf{d}}_i = \begin{Bmatrix} w^i \\ w_{,\xi}^i \\ w_{,\eta}^i \\ w_{,\xi\xi}^i \\ w_{,\eta\eta}^i \\ w_{,\xi\eta}^i \end{Bmatrix} \tag{4.8}$$

$$\mathbf{A} = \begin{bmatrix} \bar{\mathbf{A}} & \mathbf{0} & \mathbf{0} & \mathbf{0} \\ \mathbf{0} & \bar{\mathbf{A}} & \mathbf{0} & \mathbf{0} \\ \mathbf{0} & \mathbf{0} & \bar{\mathbf{A}} & \mathbf{0} \\ \mathbf{0} & \mathbf{0} & \mathbf{0} & \bar{\mathbf{A}} \end{bmatrix}, \bar{\mathbf{A}} = \begin{bmatrix} 1 & 0 & 0 & 0 & 0 & 0 \\ 0 & j_{11} & j_{12} & 0 & 0 & 0 \\ 0 & j_{21} & j_{22} & 0 & 0 & 0 \\ 0 & j_{22,\xi} & j_{12,\xi} & j_{11}^2 & j_{12}^2 & 2j_{11}j_{12} \\ 0 & j_{21,\eta} & j_{11,\eta} & j_{21}^2 & j_{22}^2 & 2j_{21}j_{22} \\ 0 & j_{22,\eta} & j_{12,\xi} & j_{11}j_{12} & j_{21}j_{22} & (j_{11}j_{22} + j_{12}j_{21}) \end{bmatrix} \tag{4.9}$$

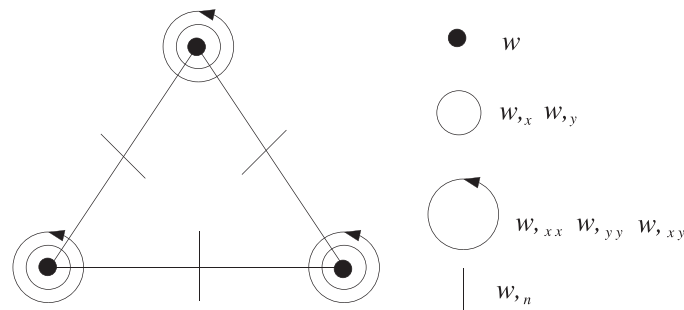


Figure 10. Degrees of freedom of the Argyris triangular finite element.

5. HIERARCHICAL HIGH-ORDER TRIANGULAR ELEMENT

The Argyris triangle illustrated in Figure 10 is a C^1 fifth-order conforming element with 21 degrees of freedom according to the Pascal triangle [10]. Each vertex has 6 degrees of freedom related to $w, w_{,x}, w_{,y}, w_{,xx}, w_{,yy}$ and $w_{,xy}$, and each edge has one degree of freedom associated with the normal derivative $w_{,n}$.

We obtain the shape functions of a new fifth-order triangular element and high-order shape functions by the tensor product of one-dimensional functions $\phi_j(L_i)$ given in terms of the natural coordinates L_i in Figure 11 using a similar procedure presented in [5]. The one-dimensional functions $\phi_j(L_i)$ are defined as

$$\begin{aligned} \phi_1(L_i) &= 1 & \phi_4(L_i) &= L_i^3(10 - 15L_i + 6L_i^2) \\ \phi_2(L_i) &= L_i & \phi_5(L_i) &= L_i^3(4 - 3L_i) \\ \phi_3(L_i) &= \frac{1}{2}L_i^2 & \phi_6(L_i) &= L_i^3 \end{aligned} \tag{5.1}$$

The local approximation of the transversal displacement $w(L_1, L_2, L_3)$ for the fifth-order element is written as

$$w(L_1, L_2, L_3) = \underbrace{\sum_{k=1}^{18} a_k \psi_k(L_1, L_2, L_3)}_{\text{vertices}} + \underbrace{\sum_{k=19}^{21} a_k \psi_k(L_1, L_2, L_3)}_{\text{edges}} \tag{5.2}$$

The shape functions $\psi_k(L_1, L_2, L_3)$ can be written according to [5] as

$$\psi_k(L_1, L_2, L_3) = \phi_p(L_1)\phi_q(L_2)\phi_r(L_3), \quad k = 1, \dots, 21 \tag{5.3}$$

The shape functions derived by the tensor product of $\phi_j(L_i)$ are not the same functions of the Argyris triangle. Figure 12 shows the six vertex shape functions ψ_1^a to ψ_6^a . They have similar collocation properties as for the H_5 square element.

For the hierarchical high-order triangular element, the tensor product (5.3) is also used to build the edge and face shape functions for polynomial order $P \geq 6$. The edge and face functions and their first- and second-order derivatives are zero at $L_i = 0$ and $L_i = 1$. The one-dimensional hierarchical high-order functions are given by

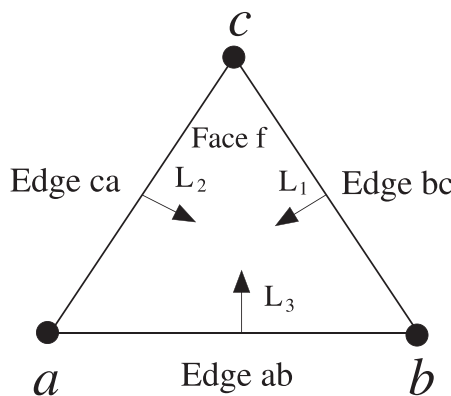


Figure 11. Natural coordinates for the triangle.

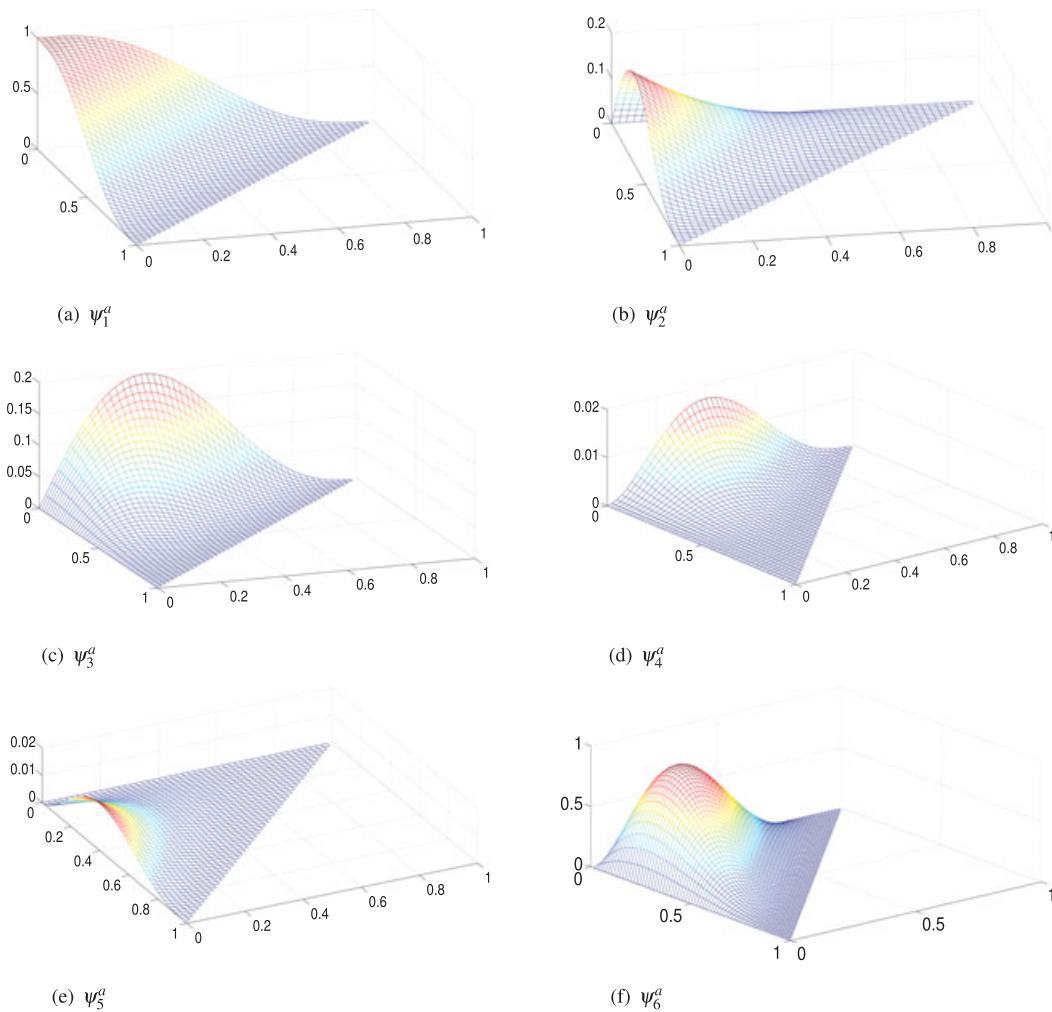


Figure 12. Vertex functions for the fifth-order triangular element.

$$\phi_{P+1}(L_i) = L_i^2 J_{P-5}^{1,1}(L_i), \quad P \geq 6, \quad i = 1, 2, 3 \tag{5.4}$$

The high-order triangular element has the same 6 degrees of freedom for each vertex and 18 vertex shape functions. The number of shape functions for each edge is $(2P - 9)$ with $P \geq 5$, and the total number of edge shape functions is $3(2P - 9)$. The number of face shape functions is $\frac{1}{2}(P - 4)(P - 5)$ for $P \geq 6$. There are 18 vertex functions, 9 edge functions and 1 face function for $P = 6$. The first edge function is associated with the normal derivative of displacement, and the second is associated with the transversal displacement. The element is global C^1 continuous and C^2 continuous on the vertices.

Table V presents the high-order tensor indices for $P = 6$. Figure 13 shows the edge and face functions for $P = 6$. The edge functions are scaled by 100 and the face functions by 1000 to achieve the same order of magnitude as the vertex functions.

The tensor indices p, q and r are calculated for $P \geq 6$ as:

- edge ab : $p = P + 1, q = 3, r = 2$ for w ; $p = P + 1, q = P + 1, r = 1$ for w_n ;
- edge bc : $p = 2, q = P + 1, r = 3$ for w ; $p = 1, q = P + 1, r = P + 1$ for w_n ;
- edge cd : $p = 3, q = 2, r = P + 1$ for w ; $p = P + 1, q = 1, r = P + 1$ for w_n ; and
- face f : $p = 3, q, r \geq P + 1$ and $q + r \leq P + 8$.

Table V. Tensor indices p, q and r for the edge and face shape functions of the high-order triangular element for $P = 6$.

| ψ | ψ_2^{ab} | ψ_2^{bc} | ψ_2^{ca} | ψ_3^{ab} | ψ_3^{bc} | ψ_3^{ca} | ψ_1^f |
|--------|---------------|---------------|---------------|---------------|---------------|---------------|------------|
| p | 7 | 2 | 3 | 7 | 1 | 7 | 3 |
| q | 3 | 7 | 2 | 7 | 7 | 1 | 7 |
| r | 2 | 3 | 7 | 1 | 7 | 7 | 7 |

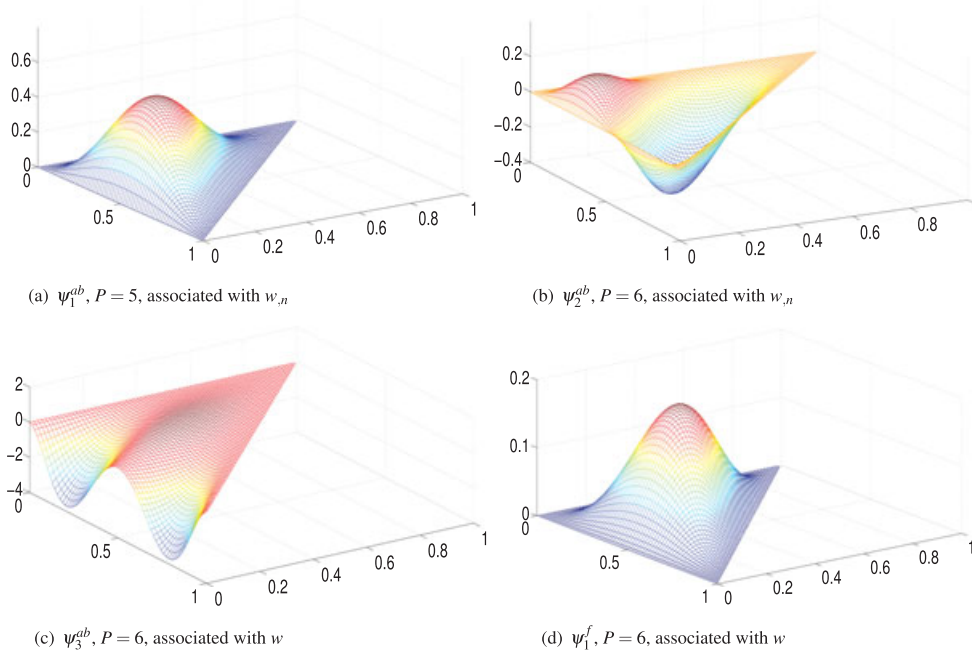


Figure 13. Edge and face shape functions of the high-order triangular element for $P = 6$.

Figure 14 shows the first edge shape function for $P = 6$, and its first- and second-order partial derivatives of two vertex shape functions associated with $w_{,xx}$ and $w_{,xy}$ for a two-triangle mesh sharing a common edge. We observe that the proposed basis is C^1 continuous.

The dependent natural coordinate of the triangle is $L_1 = 1 - L_2 - L_3$, and the approximation for the transversal displacement may be expressed in the standard domain as $w(L_2, L_3)$. The local vertex degrees of freedom of the element are $w^i, w_{,L_2}^i, w_{,L_3}^i, w_{,L_2L_2}^i, w_{,L_3L_3}^i$ and $w_{,L_2L_3}^i$. Again, the finite element stiffness matrices require the global derivatives $w^i, w_{,x}^i, w_{,y}^i, w_{,xx}^i, w_{,yy}^i$ and $w_{,xy}^i$. Therefore, we can use the mapping between the standard and physical domains, similar to Equations (3.5) and (4.7), and obtain

$$w(x, y) = \mathbf{N}_e^T \mathbf{d}_e = \mathbf{N}_e^T(L_2, L_3) \mathbf{A} \bar{\mathbf{d}}_e \tag{5.5}$$

where

$$\mathbf{d}_e = \begin{Bmatrix} \mathbf{d}_a \\ \mathbf{d}_b \\ \mathbf{d}_c \end{Bmatrix}, \mathbf{d}_i = \begin{Bmatrix} w^i \\ w_{,x}^i \\ w_{,y}^i \\ w_{,xx}^i \\ w_{,yy}^i \\ w_{,xy}^i \end{Bmatrix}, \bar{\mathbf{d}}_e = \begin{Bmatrix} \bar{\mathbf{d}}_a \\ \bar{\mathbf{d}}_b \\ \bar{\mathbf{d}}_c \end{Bmatrix}, \bar{\mathbf{d}}_i = \begin{Bmatrix} w^i \\ w_{,L_2}^i \\ w_{,L_3}^i \\ w_{,L_2L_2}^i \\ w_{,L_3L_3}^i \\ w_{,L_2L_3}^i \end{Bmatrix} \tag{5.6}$$

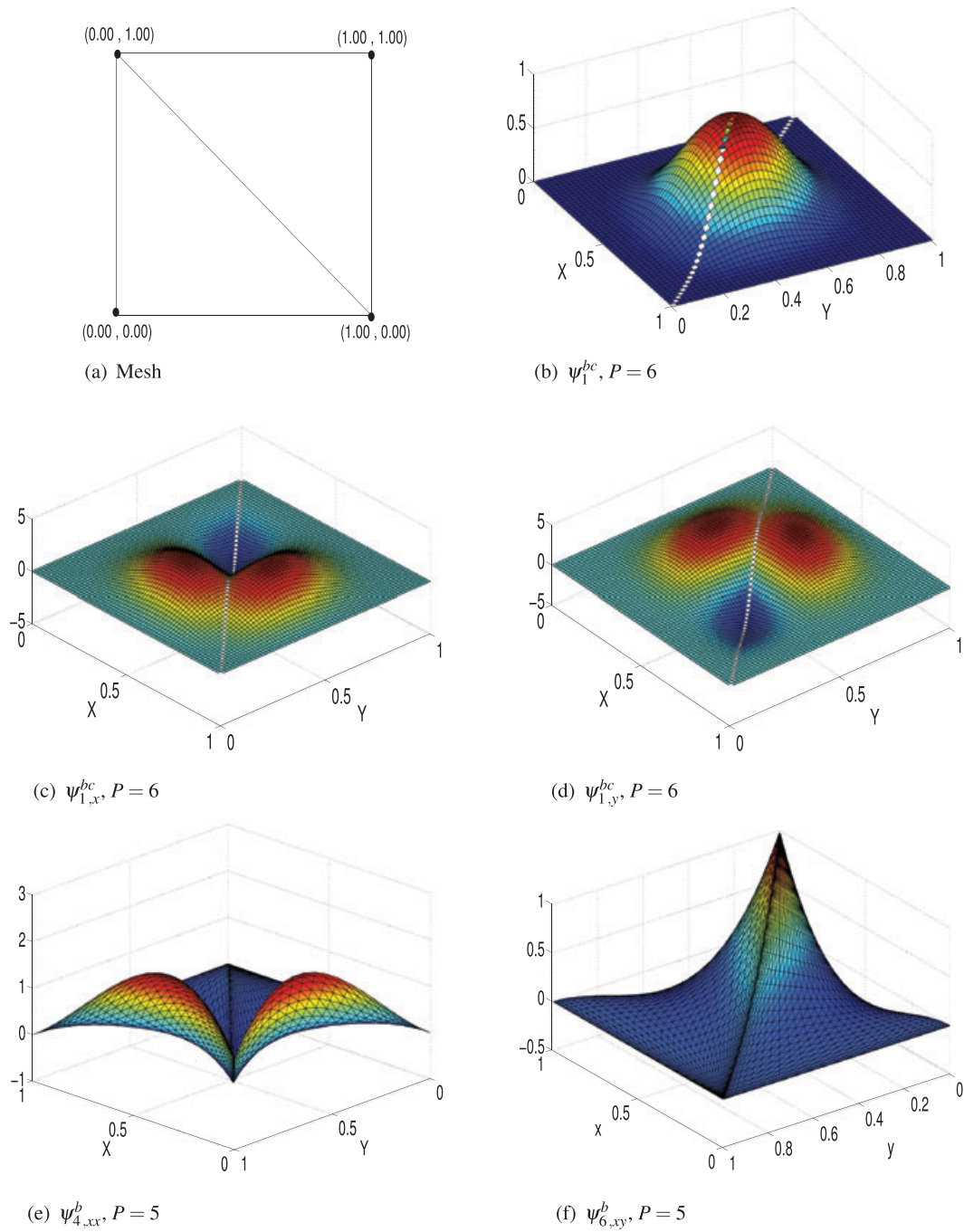


Figure 14. C^1 continuity of the shape functions on the common edge of two triangles and C^2 continuity of the vertex shape functions.

$$\mathbf{A} = \begin{bmatrix} \bar{\mathbf{A}} & \mathbf{0} & \mathbf{0} \\ \mathbf{0} & \bar{\mathbf{A}} & \mathbf{0} \\ \mathbf{0} & \mathbf{0} & \bar{\mathbf{A}} \end{bmatrix}, \quad \bar{\mathbf{A}} = \begin{bmatrix} 1 & 0 & 0 & 0 & 0 & 0 \\ 0 & j_{11} & j_{12} & 0 & 0 & 0 \\ 0 & j_{21} & j_{22} & 0 & 0 & 0 \\ 0 & 0 & 0 & j_{11}^2 & j_{12}^2 & 2 j_{11} j_{12} \\ 0 & 0 & 0 & j_{21}^2 & j_{22}^2 & 2 j_{21} j_{22} \\ 0 & 0 & 0 & j_{11} j_{12} & j_{21} j_{22} & (j_{11} j_{22} + j_{12} j_{21}) \end{bmatrix} \quad (5.7)$$

The normal derivatives on the edges are calculated as

$$w_{,n} = n_x w_{,x} + n_y w_{,y} \quad (5.8)$$

where (n_x, n_y) are the components of the normal vector \mathbf{n} on each edge and are constant for straight-sided triangles.

6. NUMERICAL RESULTS

In this section, we present numerical results for a patch test and problems with smooth fabricated solutions to validate the developed plate elements. We also present results for a plate with singularity and a transient analysis. We compare the approximation errors and the convergence rates using h - and p -refinements with non-distorted and distorted meshes of the hierarchical high-order elements: H_3 ($Quad_{H3}$), H_5 ($Quad_{H5}$) and triangle (Tri). For that purpose, we consider the rectangular plate with dimensions $[0, a] \times [0, b]$ illustrated in Figure 15.

Initially, a patch test is analysed to show that the elements recover rigid body solutions. A projection problem with polynomial solution is then considered. Plate subjected to distributed load $q(x, y)$ and two distinct sets of boundary conditions, with all edges simply supported and clamped, are analysed. The L_2 -norm of the approximation error for w and its partial derivatives and the energy norm of the error are considered in the comparative analysis of the convergence rates. They are given respectively by

$$\|e\|_{L_2} = \sqrt{\int_A (u - u_{app})^2 t dA} \quad (6.1)$$

$$\|e\|_E = \|u\|_E - \|u_{app}\|_E \quad (6.2)$$

where u and u_{app} are, respectively, the fabricated and approximated solutions. The energy norm of u is

$$\|u\|_E = \sqrt{D \int_A (u_{,xx}^2 + u_{,yy}^2 + 2\nu u_{,xx} u_{,yy} + 2(1-\nu) u_{,xy}^2) t dA} \quad (6.3)$$

6.1. Patch test

To validate the developed high-order elements, we compare the solutions of a usual patch test for plates modelled with quadrilateral and triangular elements [26]. The patch test checks if the elements are able to reproduce constant values for all degrees of freedom with non-distorted and distorted meshes. It is important that the considered mesh elements have enough neighbours to recover correctly the rigid body motion. The boundary deflections are given by $w(x, y) = \frac{1}{2}(1 + x + 2y + x^2 + xy + y^2)$ as in [26], with $E = 109.2$ GPa, $\nu = 0.3$ and thickness $t = 0.01$ m.

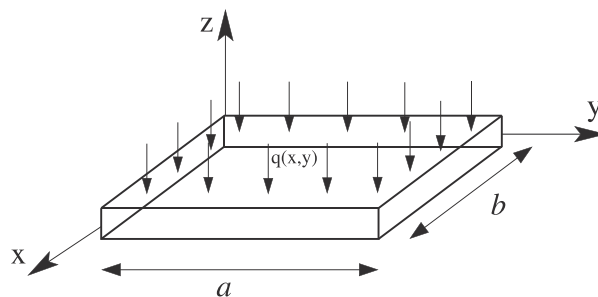


Figure 15. Rectangular plate subjected to distributed load.

The distorted meshes for triangles and quadrilaterals have, respectively, 5 and 10 elements and are illustrated in Figure 16. The degrees of freedom values for node 5 are presented in Table VI. The results were obtained with polynomial orders 3, 5 and 5, respectively, for the H_3 and H_5 quadrangular and triangular elements. We can observe that the proposed elements passed the patch test, and they are able to reproduce rigid body motion.

6.2. Projection problem

The function considered for the projection problem is $f(x, y) = x^3(x - 1)^3 y^3(y - 1)^3$ in the domain $[0, 1] \times [0, 1]$. A polynomial function was chosen in order to achieve an approximation error close to zero when the order of the interpolation functions is equal to the respective order of the given function. In this way, we can compare more clearly the effects of mesh distortion for the proposed elements. The distorted and non-distorted meshes used in the h -refinement have 4, 9, 16 and 25 quadrilaterals and 8, 18, 32 and 50 triangles. The quadrilateral and triangular meshes are shown in Figures 17 and 18, respectively. The non-distorted meshes are similar. The element orders were fixed in $P = 3$ for the H_3 square and $P = 5$ for the H_5 quadrilateral and triangle.

For the p -refinement, we used the mesh with four H_3 square elements and increased the polynomial order from $P = 3$, which corresponds to the BFS element, to $P = 13$. For the hierarchical high-order H_5 quadrilateral element, we also used the mesh with four elements and increased the polynomial order from $P = 5$ to $P = 7$. For the hierarchical high-order triangle, we used the mesh with eight elements and increased the polynomial order from $P = 5$ to $P = 12$.

The L_2 -error norm for the transversal displacement w and its first- ($w_{,x}$) and second-order ($w_{,xy}$) partial derivatives obtained using the non-distorted and distorted meshes in terms of the number of degrees of freedom and logarithm scales are shown in Figures 19–21. Similar plots were obtained for $w_{,y}$, $w_{,xx}$ and $w_{,yy}$.

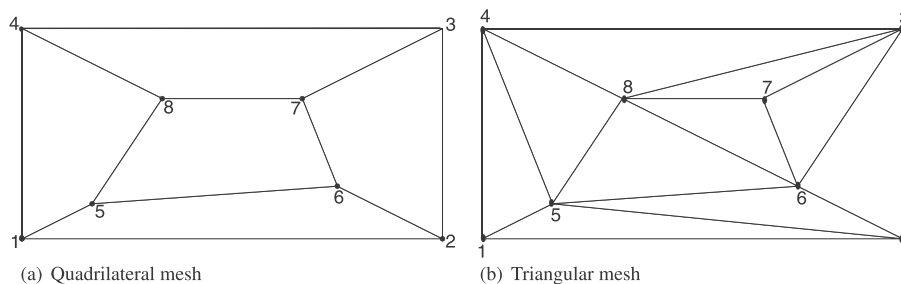


Figure 16. Distorted meshes for the patch test [26].

Table VI. Results for node 5 of the patch test with distorted meshes.

| Element | w | $w_{,x}$ | $w_{,y}$ | $w_{,xx}$ | $w_{,yy}$ | $w_{,xy}$ |
|----------------|--------|----------|----------|-----------|-----------|-----------|
| $Quad_{H_3}$ | 0.5414 | 1.0400 | -0.5500 | -0.0111 | -0.0111 | -0.0033 |
| $Quad_{H_5}$ | 0.5414 | 1.0400 | -0.5500 | -0.0111 | -0.0111 | -0.0033 |
| Tri | 0.5414 | 1.0400 | -0.5500 | -0.0111 | -0.0111 | -0.0033 |
| Reference [26] | 0.5414 | 1.0400 | -0.5500 | -0.0111 | -0.0111 | -0.0033 |

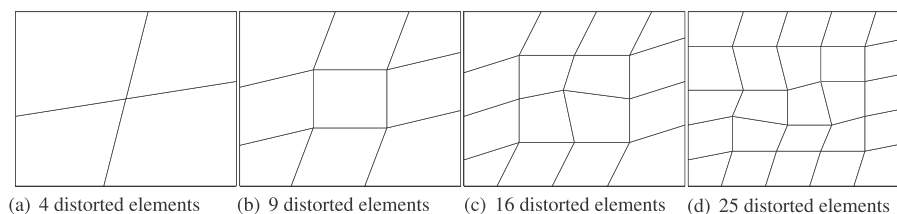


Figure 17. Quadrilateral meshes used in the projection problem.

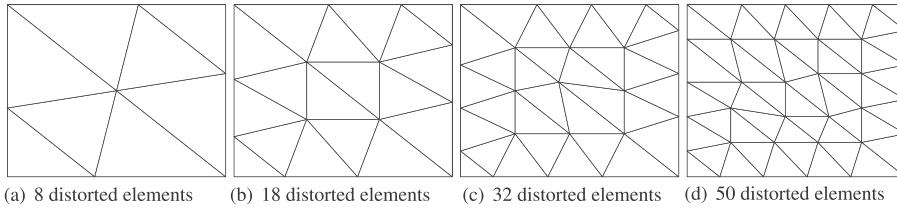


Figure 18. Triangular meshes used in the projection problem.

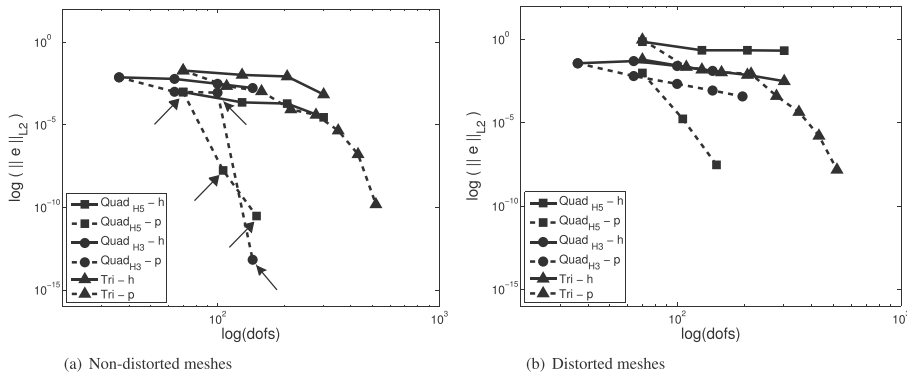


Figure 19. L_2 -error norm of w for the projection problem.

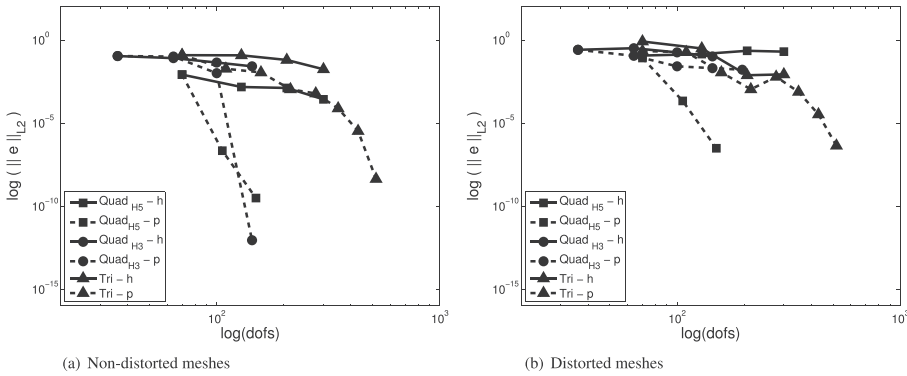


Figure 20. L_2 -error norm of w_x for the projection problem.

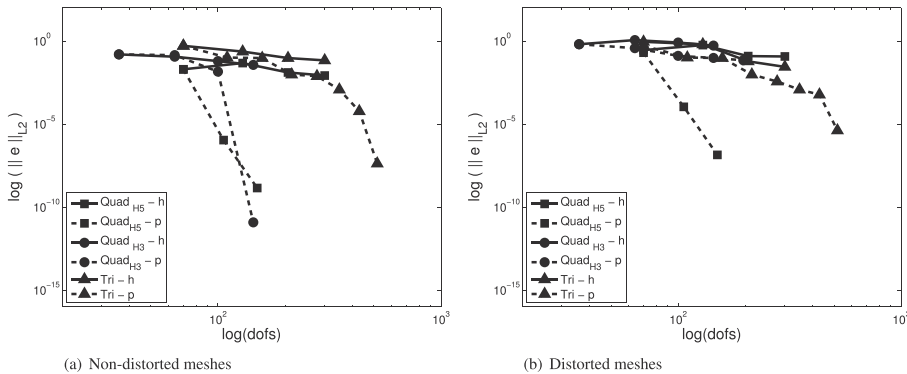


Figure 21. L_2 -error norm of $w_{,xy}$ for the projection problem.

Table VII. Absolute values of the angular coefficients of the fitted straight lines for the L_2 -error norms for the projection problem.

| (a) Non-distorted meshes | | | | | | |
|--------------------------|-------|-------|-------|----------|----------|----------|
| Element | w | w_x | w_y | w_{xx} | w_{yy} | w_{xy} |
| $Quad_{H_3} - h$ | 1.08 | 1.04 | 1.04 | — | — | 1.05 |
| $Quad_{H_5} - h$ | 2.18 | 2.14 | 2.14 | 2.31 | 2.31 | 2.31 |
| $Tri - h$ | 2.00 | 1.26 | 1.33 | 1.43 | 1.51 | 1.51 |
| $Quad_{H_3} - p$ | 22.56 | 22.93 | 22.85 | — | — | 20.87 |
| $Quad_{H_5} - p$ | 16.57 | 16.16 | 16.73 | 14.80 | 16.56 | 15.35 |
| $Tri - p$ | 11.59 | 10.76 | 10.75 | 9.76 | 10.54 | 9.75 |
| (b) Distorted meshes | | | | | | |
| Element | w | w_x | w_y | w_{xx} | w_{yy} | w_{xy} |
| $Quad_{H_3} - h$ | 0.76 | 0.68 | 0.62 | — | — | 0.14 |
| $Quad_{H_5} - h$ | 2.77 | 1.97 | 2.09 | 2.59 | 2.87 | 3.07 |
| $Tri - h$ | 2.99 | 3.58 | 3.42 | 2.58 | 3.62 | 3.52 |
| $Quad_{H_3} - p$ | 2.66 | 1.53 | 1.53 | — | — | 1.29 |
| $Quad_{H_5} - p$ | 16.60 | 16.34 | 17.09 | 18.58 | 18.19 | 17.66 |
| $Tri - p$ | 7.83 | 5.72 | 5.72 | 4.95 | 5.01 | 5.01 |

The angular coefficients of the fitted straight lines in logarithmic scale for the L_2 -error norms of w , w_x , w_y , w_{xx} , w_{yy} and w_{xy} were calculated for the non-distorted and distorted meshes using the polyfit MATLAB function. The absolute values of the angular coefficients give the convergence rates for the h - and p -refinements and are presented in Table VII.

The p -refinement has better convergence rates than h -refinement for all elements in distorted and non-distorted meshes. The H_3 and H_5 squares have better convergence rates than the triangle for non-distorted meshes. These elements require a smaller number of degrees of freedom to achieve the same error magnitude. This is expected because the approximation in the triangle is poorer compared with the square elements. For example, the term $x^6 y^6$ in the triangle only appears from expansion order $P = 12$, and for square elements, this term appears from $P = 6$. For distorted meshes, the H_5 square has almost the same convergence rates as the non-distorted meshes, but the rates dropped approximately 50% for triangles. The H_3 square has worse convergence rates compared with the results of non-distorted meshes. The convergence rates for w and its first- and second-order derivatives were exponential using the H_3 square with non-distorted meshes and the H_5 and triangular elements with non-distorted and distorted meshes. The H_5 quadrilateral also recovered the second-order derivatives very well, even for distorted meshes. Despite being C^1 global continuous, the triangle recovered the second-order derivatives well, with good convergence rates.

Recently, problems described by sixth-order equations have received more attention such as growth of crystalline surfaces, oil-water-surfactant mixtures and mixtures of polymer molecules [27]. The conforming finite element approximation of sixth-order equations requires C^2 continuity. Although the bases presented here for the H_5 and triangular elements are C^1 continuous on the element edges and C^2 continuous only on the element vertices, we observed good approximation errors for the second derivatives. Therefore, these elements may obtain reasonable results even for sixth-order equations.

The behaviour of the condition numbers of the Schur complemented mass matrices for the hierarchical high-order H_3 and H_5 squares and the triangular element are shown in Figure 22(a). The H_3 square element has condition numbers greater than the H_5 square and triangular elements for $P \geq 5$. The H_5 square element has a smaller condition number than the triangular element from $P = 5$ to $P = 8$. For $P = 9$ and $P = 10$, both elements obtains almost the same condition numbers. For $P \geq 10$, the inverse behaviour is observed, and the triangle has smaller condition numbers than the H_5 square element. The H_3 square element exhibits an almost constant increasing rate of condition number when the other elements have some variations in the increasing rate. The largest condition number is for the H_3 square element and $P = 12$ with magnitude of 10^{11} . Figure 22(b) shows the condition numbers of the element stiffness matrices for the considered bases. They are lower than the condition numbers of the mass matrices, and the increasing rates are moderate for all elements.

6.3. Rectangular simply supported plate

The rectangular plate shown in Figure 15 with simply supported edges has dimensions $a = 4$ m, $b = 4$ m, thickness $t = 0.01$ m, Young’s modulus $E = 109.2$ GPa and Poisson’s ratio $\nu = 0.3$. The plate is loaded with $q(x, y) = q_0 \sin(\frac{\pi x}{4}) \sin(\frac{\pi y}{4})$ and $q_0 = 100 \frac{N}{m^2}$. The analytical solution is given by

$$w(x, y) = \frac{q_0}{\pi^4 D (\frac{1}{a^2} + \frac{1}{b^2})} \sin\left(\frac{\pi x}{a}\right) \sin\left(\frac{\pi y}{b}\right) \tag{6.4}$$

The boundary conditions for the simply supported edges are

- edge $x = 0$: $w(0, y) = 0, w_{,x}(0, y) = 0, M_{nn} = M_{xx}$ and $M_{nt} = M_{xy}$;
- edge $x = a$: $w(a, y) = 0, w_{,x}(a, y) = 0, M_{nn} = M_{xx}$ and $M_{nt} = M_{xy}$;
- edge $y = 0$: $w(x, 0) = 0, w_{,y}(x, 0) = 0, M_{nn} = M_{yy}$ and $M_{nt} = -M_{xy}$;
- edge $y = b$: $w(x, b) = 0, w_{,y}(x, b) = 0, M_{nn} = M_{yy}$ and $M_{nt} = -M_{xy}$.

The analytical expressions for $w_{,x}, w_{,y}, w_{,xy}, w_{,xx}$ and $w_{,yy}$ can be obtained from the derivatives of Equation (6.4). The boundary moments M_{xx}, M_{yy} and M_{xy} are calculated using Equations (2.5) to (2.7).

The h -refinement for the BFS square element considered non-distorted meshes with 4, 16, 36, 64, 100 and 144 elements. Figure 23(a) and (b) shows the coarsest and the finest meshes. For p -refinement using the H_3 square element, we fixed the mesh with four elements and increased the polynomial orders from $P = 3$, which corresponds to the BFS element, to $P = 13$. The finest mesh used in the h -refinement has the same number of degrees of freedom as the p -refinement for order $P = 13$.

The h -refinement for the H_5 high-order square element used non-distorted meshes with 2, 4, 9 and 16 elements. For the p -refinement, we used the non-distorted mesh with two elements and increased the polynomial orders from $P = 5$ to $P = 12$. For triangular elements, the h -refinement considered non-distorted meshes of 2, 4, 8, 16 and 32 elements. For the p -refinement, we used the mesh with four elements and increased the polynomial orders from $P = 5$ to $P = 12$. For distorted

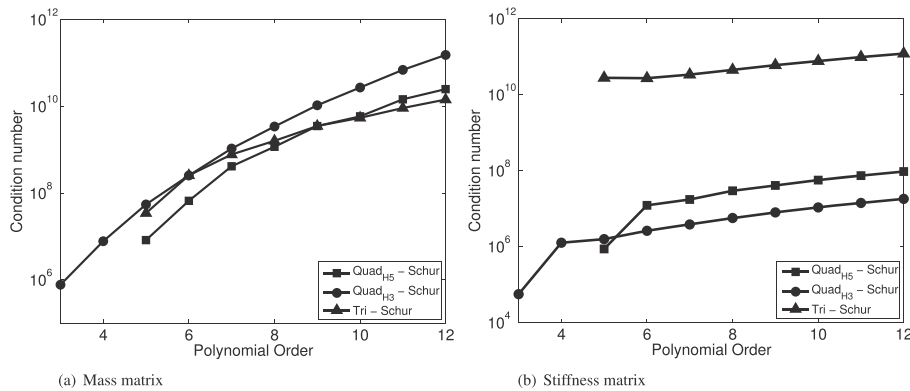


Figure 22. Condition numbers of the Schur complemented mass and stiffness matrices for the hierarchical high-order elements.

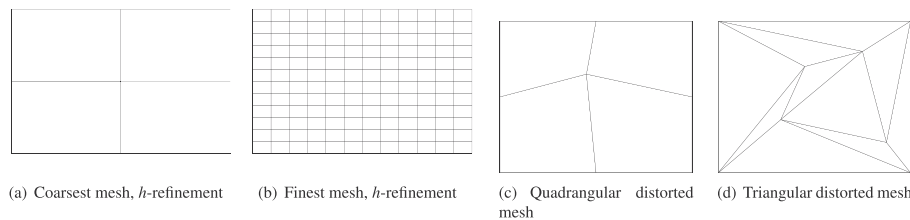


Figure 23. Meshes used for the analysis of the rectangular plates.

meshes, only p -refinement is considered with polynomial orders from $P = 5$ to $P = 12$, and the meshes for the H_3 and H_5 quadrilaterals and the triangle are shown respectively in Figure 23(c) and (d).

The L_2 -norm of the approximation errors for the transversal displacement and its first- and second-order partial derivatives for non-distorted and distorted meshes were calculated. The convergence rates, given by the absolute values of the angular coefficients of the fitted straight lines in logarithmic scale, for the L_2 - and energy error norms, are given in Table VIII. Figure 24 shows the results in terms of the energy norm.

The results show that the p -refinement converges faster than h -refinement for distorted and non-distorted meshes, similarly to the projection problem of the previous section. The convergence rates for the H_3 square element are better than the convergence rates of the H_5 square and triangle for h - and p -refinements with non-distorted meshes. For distorted meshes, the convergence rates for the H_3 square deteriorated because of the loss of C^1 continuity. The convergence rates for the H_5 square and triangle are close for non-distorted meshes. For distorted meshes, the H_5 square behaviour is better than the triangle, and smaller error norms are achieved with a smaller number of degrees of freedom. For p -refinement, the convergence rates with non-distorted meshes for all elements are exponential. For distorted meshes, the convergence rates are almost exponential only for the H_5 and triangle, and there is a good recovery of the second-order derivatives of w .

6.4. Rectangular clamped plate

The rectangular plate of Figure 15 with clamped edges has dimensions $a = 1$ m, $b = 1$ m, thickness $t = 0.01$ m, Young's modulus $E = 109.2$ GPa and Poisson's ratio $\nu = 0.3$. The boundary conditions for the clamped edges are

Table VIII. Absolute values of the angular coefficients of error norms for the simply supported plate.

| (a) Non-distorted meshes | | | | | | | |
|--------------------------|--------|-------|-------|-------|--------|--------|--------|
| Element | Energy | w | w,x | w,y | w,xx | w,yy | w,xy |
| $Quad_{H_3} - h$ | 2.35 | 2.41 | 1.80 | 1.80 | — | — | 1.78 |
| $Quad_{H_5} - h$ | 2.03 | 3.88 | 2.11 | 1.87 | 2.06 | 2.06 | 1.14 |
| $Tri - h$ | 2.28 | 2.31 | 2.27 | 2.24 | 2.26 | 2.26 | 2.31 |
| $Quad_{H_3} - p$ | 11.67 | 10.75 | 10.32 | 10.32 | — | — | 10.10 |
| $Quad_{H_5} - p$ | 9.02 | 9.44 | 9.41 | 7.90 | 9.21 | 9.28 | 8.56 |
| $Tri - p$ | 5.97 | 9.58 | 6.97 | 6.99 | 7.83 | 9.05 | 7.69 |
| (b) Distorted meshes | | | | | | | |
| Element | Energy | w | w,x | w,y | w,xx | w,yy | w,xy |
| $Quad_{H_3} - p$ | 0.53 | 0.14 | 0.03 | 0.05 | — | — | 0.17 |
| $Quad_{H_5} - p$ | 5.95 | 7.21 | 6.26 | 6.26 | 6.73 | 5.17 | 5.74 |
| $Tri - p$ | 5.46 | 6.15 | 5.23 | 5.02 | 4.57 | 4.64 | 4.29 |

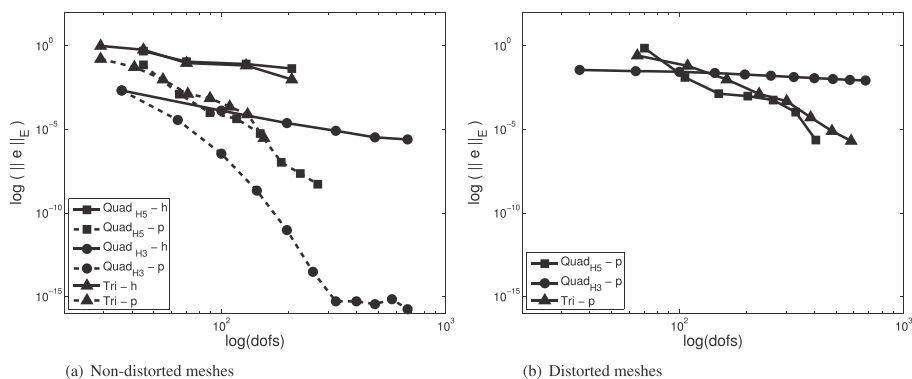


Figure 24. Error in the energy norm for the simply supported plate.

- edge $x = 0$: $w(0, y) = 0, w_x(0, y) = 0, w_{xx}(0, y) = 0, w_{xy}(0, y) = 0$;
- edge $x = a$: $w(a, y) = 0, w_x(a, y) = 0, w_{xx}(a, y) = 0, w_{xy}(a, y) = 0$;
- edge $y = 0$: $w(x, 0) = 0, w_y(x, 0) = 0, w_{yy}(x, 0) = 0, w_{xy}(x, 0) = 0$;
- edge $y = b$: $w(x, b) = 0, w_y(x, b) = 0, w_{yy}(x, b) = 0, w_{xy}(x, b) = 0$.

We consider the following fabricated solution for this analysis:

$$w(x, y) = \frac{1}{D} x^3 y^3 (x - 1)^3 (y - 1)^3 \tag{6.5}$$

Expressions for w_x, w_y, w_{xy}, w_{xx} and w_{yy} can be obtained from the derivatives of equation (6.5). Distributed load q is obtained by replacing the fourth-order derivative of w in the bi-harmonic Equation (2.2) and solving for $q(x, y)$.

The same meshes used in the h - and p -refinements for the simply supported plate are used to solve this problem. Results for the L_2 -norm of the approximation errors for w and its first- and second-order partial derivatives were calculated, and the errors in the energy norm for the non-distorted and distorted meshes are shown in Figure 25. The absolute values of the angular coefficients for the fitted straight lines in logarithmic scale for the L_2 - and energy error norms for non-distorted and distorted meshes are shown in Table IX.

As in the previous problems, the p -refinement achieved exponential convergence rates for non-distorted meshes for the three elements. The rates are still exponential for the H_5 square and triangle for the distorted meshes, including the second-order partial derivatives. For distorted meshes, the H_5 quadrilateral element was more accurate than the other elements with better convergence rates.

The fabricated solution (6.5) is the same function used in the projection problem of Section 6.2 for $D = 1$. In this sense, the plate and projection problems are equivalent and the respective coefficients of the approximated solutions should be the same. The projection problem does not require

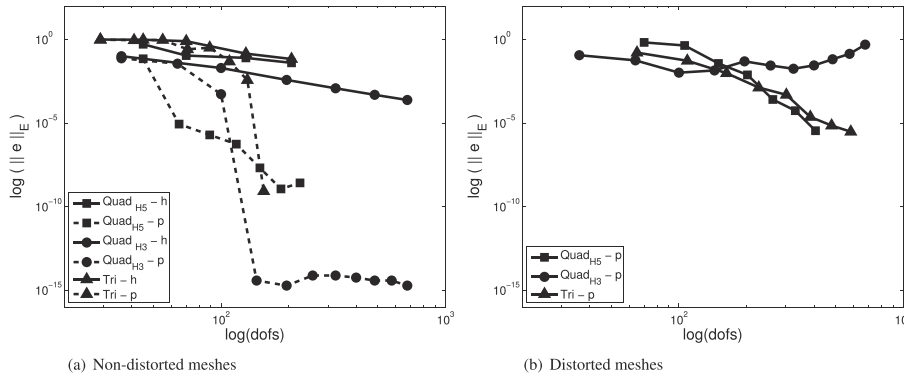


Figure 25. Error in the energy norm for the clamped plate.

Table IX. Absolute values of the angular coefficients of error norms for the clamped plate.

| (a) Non-distorted meshes | | | | | | | |
|--------------------------|--------|------|-------|-------|----------|----------|----------|
| Element | Energy | w | w_x | w_y | w_{xx} | w_{yy} | w_{xy} |
| $Quad_{H_3} - h$ | 2.11 | 2.19 | 1.61 | 1.61 | — | — | 1.59 |
| $Quad_{H_5} - h$ | 1.51 | 3.06 | 1.67 | 1.66 | 1.94 | 1.94 | 2.49 |
| $Tri - h$ | 1.49 | 1.56 | 1.52 | 1.53 | 1.43 | 1.43 | 1.58 |
| $Quad_{H_3} - p$ | 12.93 | 8.98 | 8.30 | 8.30 | — | — | 8.22 |
| $Quad_{H_5} - p$ | 10.67 | 5.97 | 6.33 | 5.12 | 5.45 | 5.45 | 7.00 |
| $Tri - p$ | 8.57 | 9.10 | 8.41 | 8.25 | 7.27 | 7.55 | 7.34 |
| (b) Distorted meshes | | | | | | | |
| Element | Energy | w | w_x | w_y | w_{xx} | w_{yy} | w_{xy} |
| $Quad_{H_3} - p$ | 0.69 | 0.40 | 0.12 | 0.22 | — | — | 0.03 |
| $Quad_{H_5} - p$ | 10.13 | 7.69 | 7.99 | 8.70 | 7.32 | 7.67 | 7.93 |
| $Tri - p$ | 5.32 | 6.15 | 5.23 | 5.02 | 4.57 | 4.64 | 4.29 |

the application of boundary conditions because the mass matrix is positive definite and the projected function contains information regarding its behaviour on the domain boundary. The boundary conditions need to be applied for the clamped plate problem, and the transversal displacement and its derivatives are zero on the boundary as indicated previously. However, whereas the coefficients of the approximated solutions associated with the edge and face functions are equal for the projection and plate problems, a small difference exists in the coefficients of the vertex shape functions. Despite the fact that the values associated with the degrees of freedom of the boundary conditions are imposed as zero for the plate, the projection problem recovered non-zero coefficients, and they represent optimal values for the considered approximation spaces. This explains the difference in the convergence rates indicated in Tables VII and IX. A similar conclusion is valid for the simply supported plate.

The a priori error estimate in the H_2 norm for a smooth analytical solution is given by [28]

$$\|e\|_{H_2} = C(u)h^{P-1}e^{-bP} \tag{6.6}$$

where $b > 0$ is a constant dependent on the considered problem,

For two successive orders P_i and P_{i+1} , the convergence rate is determined as

$$\zeta = \frac{\|e_i\|_{H_2}}{\|e_{i+1}\|_{H_2}} = \frac{h_i^{P_i-1}}{h_{i+1}^{P_{i+1}-1}} \frac{e^{-b P_i}}{e^{-b P_{i+1}}} \tag{6.7}$$

We can simplify (6.7) for h -refinement assuming that $P_i = P_{i+1}$ as

$$\zeta = \left(\frac{h_i}{h_{i+1}}\right)^{P-1} \tag{6.8}$$

For p -refinement, we have $h_{i+1} = h_i = h$, and Equation (6.7) simplifies to

$$\zeta = \frac{e^b}{h} \tag{6.9}$$

Table X gives the convergence rates calculated using Equations (6.8) and (6.9) for the h - and p -refinements with non-distorted meshes. Because of the equivalence of the projection and plate problems and the improved accuracy of the former, the L_2 -error norms for w were used. For the H_3 square and h -refinement, the largest ratio of the characteristic element sizes for two successive meshes ($h_i = 2h_{i+1}$) was used. For the other elements, the average of ratios of the characteristic element sizes calculated for two successive refinements was considered. The values of the *calculated* column are the averages of the ratio of errors between two successive refinements. The values b used in Equation (6.9) for the p -refinement correspond to the absolute value of the angular coefficients of the fitted straight lines in logarithmic scale using the results where a greater slope exists (see the arrows in Figure 19 that indicate the cases considered for the H_3 and H_5 elements and are similar to the triangle). The convergence rates for the p -refinement in the *calculated* column are given by the ratio between the first and last approximation errors for w in the projection problem. The procedures considered allowed for comparison of the estimated convergence rates obtained from

Table X. Comparison between estimated and numerical convergence rates.

| Element | Equation (6.8) | Calculated |
|------------------|---------------------------------------|---------------------------------------|
| $Quad_{H_3} - h$ | 4.00 | 3.96 |
| $Quad_{H_5} - h$ | 8.07 | 6.79 |
| $Tri - h$ | 16.00 | 12.21 |
| Element | Equation (6.9) | Calculated |
| $Quad_{H_3} - p$ | 2.44×10^{12} ($b = 27.82$) | 1.11×10^{11} ($b = 24.74$) |
| $Quad_{H_5} - p$ | 1.78×10^8 ($b = 18.30$) | 3.23×10^7 ($b = 16.60$) |
| $Tri - p$ | 5.12×10^8 ($b = 17.97$) | 1.27×10^8 ($b = 19.36$) |

Equation (6.7) and those calculated using the h - and p -refinements. The rates for the three elements in the p -refinement are exponential.

Figure 26 shows the error in energy norm for the clamped plate using hp -refinement for quadrilateral meshes of Figure 17(a), (b) and (c) and triangular meshes of Figure 18(a), (b) and (c). For this problem with smooth solution, the p -refinement achieved optimal behaviour for the error decrease in terms of the number of degrees of freedom.

6.5. Plate with singularity

Consider the L-shaped domain illustrated in Figure 27 with the given dimensions, Young's modulus $E = 109.2$ GPa, Poisson ratio $\nu = 0.3$ and thickness $t = 0.01$ m. The external edges of the domain are all simply supported, and a constant transversal distributed load of intensity $q_0 = 100$ N/m² is applied. We will follow a similar procedure adopted in [29] for a plane strain model.

We considered five sets of meshes for the h - and p -refinements. The first set is a sequence of three uniformly refined meshes with 1587, 11 907 and 30 000 elements and, respectively, 6720, 48 640 and 121 604 degrees of freedom used for the h -refinement with the H_3 element. The coarsest mesh is illustrated in Figure 28(a). The second set is a sequence of three refined meshes closed to the singular point with 473, 806 and 4888 elements used for the h -refinement with the triangle. The coarsest mesh is illustrated in Figure 28(b), and there are 12 938, 21 845 and 131 203 degrees of

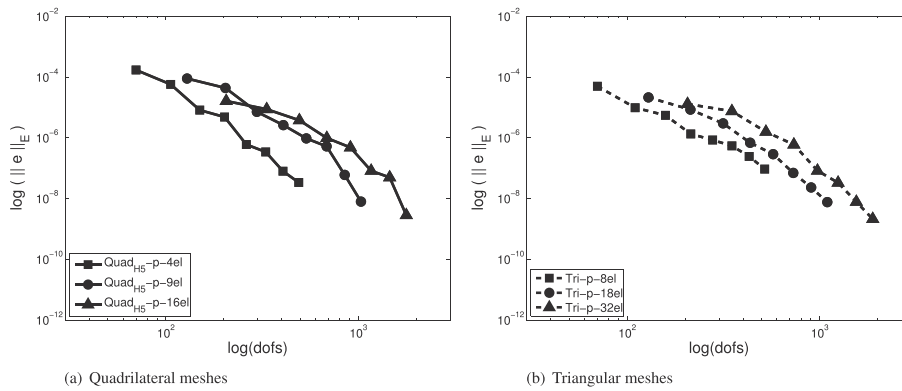


Figure 26. Error in the energy norm for the clamped plate using hp -refinement.

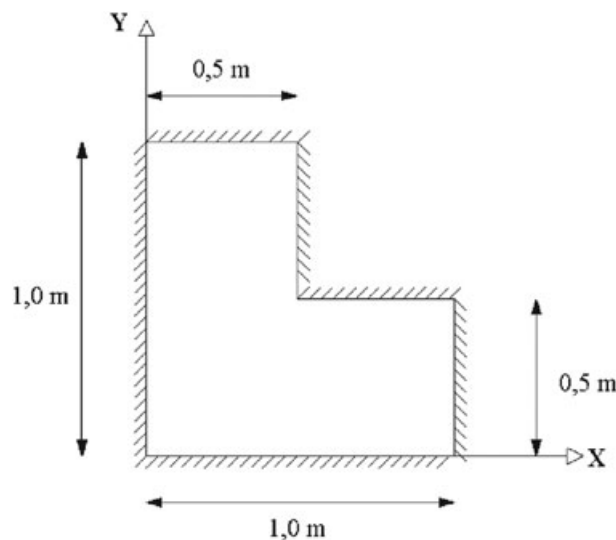


Figure 27. L-shaped domain for the plate with singularity.

freedom. The p -refinement with the H_3 element used the mesh of Figure 28(c) with 96 elements and 12 104 degrees of freedom for $P = 12$. Finally, the p -refinement with the triangle used the mesh of Figure 28(d) and the geometrical mesh of Figure 28(e) with, respectively, 192 elements and 20 516 degrees of freedom and 60 elements and 6564 degrees of freedom for $P = 12$.

The reference solution for the energy norm U_r was taken for the finest mesh of the h -refinement with the H_3 element. The percentage relative errors e_r between U_r and the energy norms U_i obtained with the other meshes were calculated as

$$e_r = \frac{|U_r - U_i|}{U_r} \times 100\% \tag{6.10}$$

Figure 29 illustrates the behaviour of the h - and p -refinements for the meshes of the H_3 and triangular elements. The h -refinements recovered the same errors for the meshes of squares and

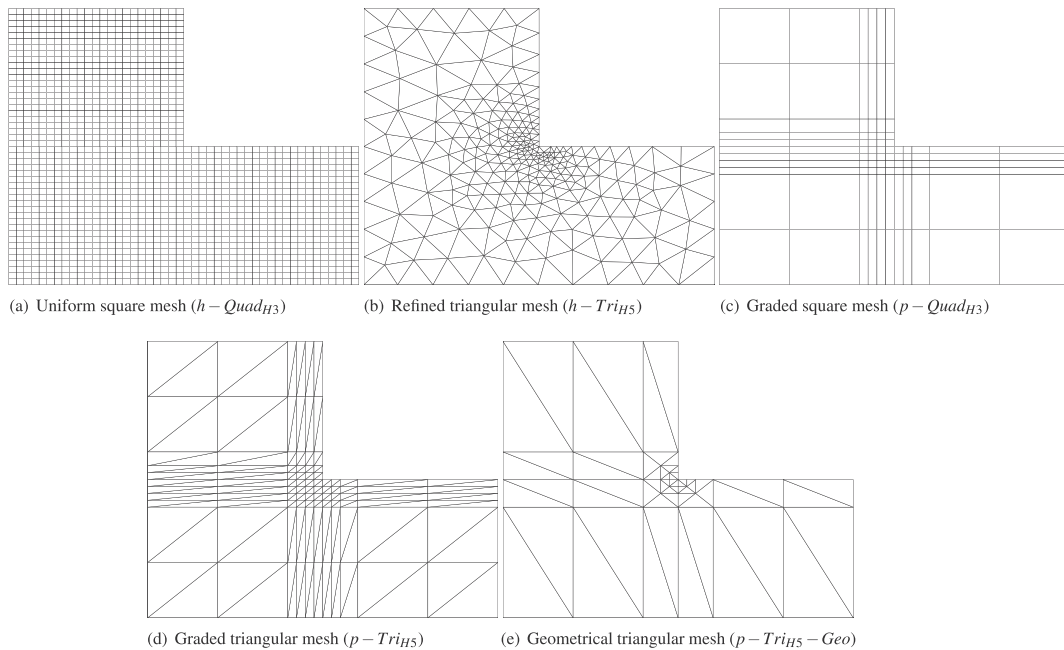


Figure 28. Meshes used for the plate with singularity.

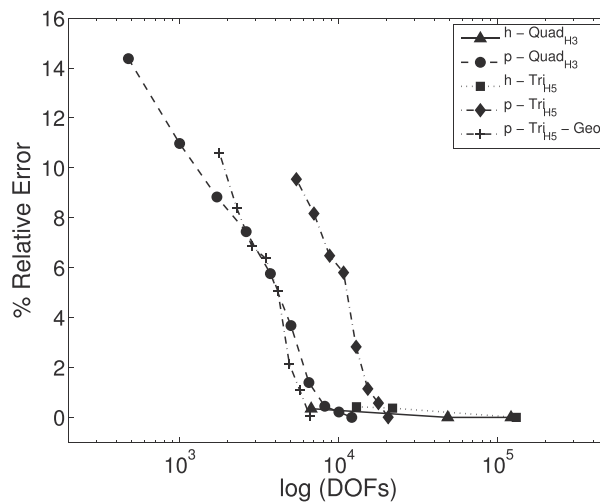


Figure 29. Error in the energy norm for the plate with singularity.

triangles. We observe that the p -refinement achieved the same errors with less degrees of freedom than the h -refinement. The average angular coefficients of the relative errors in logarithmic scale for the p -refinement are 5.03 for the square mesh of Figure 28(c), 6.65 for the triangular mesh of Figure 28(d) and 4.61 for the triangular mesh of Figure 28(e). The p -refinements worked well for this singular problem, and the best convergence rate was obtained for the graded triangular mesh of Figure 28(d).

6.6. Transient analysis

To evaluate the performance of the proposed elements in transient problems, we solved the rectangular simply supported plate of Section 6.3 under sinusoidal distributed load $q(x, y) = 100(x^2y^2) \sin(\omega_p T)$ with $E = 109.2$ GPa, $\nu = 0.3$ and thickness $t = 0.01$ m, where the frequency of excitation is $\omega_p = 20$ Hz close to the natural frequency of the considered plate $\omega = 19.7$ Hz. In this way, it is expected that deformed shape will change significantly, and the effect of p -refinement on displacements and stress components can be better observed. The time interval is $T = [0, 2]$ s with 10 000 time steps for the implicit Newmark method.

We considered the same distorted meshes of the projection problem illustrated in Figures 17(a) and 18(a) and polynomials orders 3, 5, 7 and 9 for the H_3 quadrilateral and 5, 7 and 9 for the H_5 quadrilateral and triangle. The displacements and stress components of the central node and the error in the energy norm were considered to verify the convergence. The relative errors for displacement and stress components are calculated using the displacement and stresses obtained with the finest regular mesh with 144 elements and $P = 8$. The results are presented in Figure 30 for the transversal displacement w and normal (σ_{yy}) and shear (τ_{xy}) stress components. Table XI presents the convergence rates for the energy error norm given by the angular coefficients of the fitted lines. We can observe that the H_5 quadrilateral and triangular elements had better convergence rates to the error in the energy norm. The results for the H_3 element are worse because of the mesh distortion.

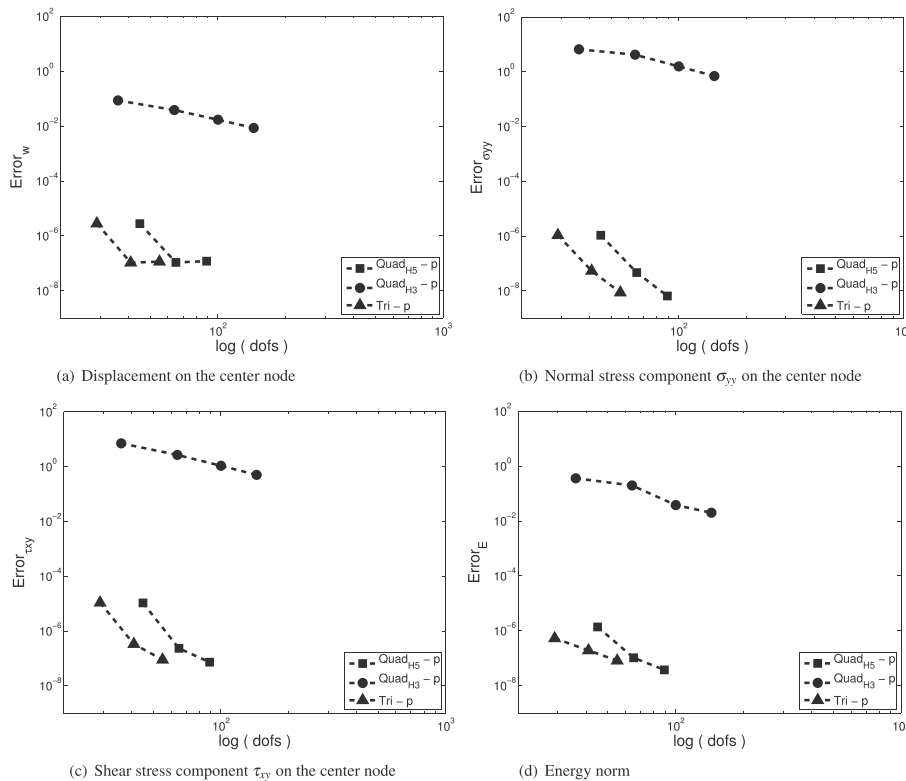


Figure 30. Errors for displacement, stress components and energy norm for the transient plate analysis.

Table XI. Rates of convergence for the energy error norm for the transient plate analysis.

| Element | Rate |
|--------------|------|
| $Quad_{H_3}$ | 0.51 |
| $Quad_{H_5}$ | 3.95 |
| Tri | 4.18 |

7. CONCLUSIONS

We presented the construction of C^1 high-order conforming finite bases applied to the solution of the Kirchhoff plate based on the tensor product of one-dimensional polynomial bases and investigated the convergence rates of the respective finite elements. Results for a patch test, projection, static and transient plate problems with smooth fabricated solutions were presented. The equivalence between the projection and plate problems was discussed, and the obtained convergence rates were compared with the estimated theoretical rates. The analysis of h - and p -refinements for a singular plate in a L-shaped domain was also considered.

The H_3 high-order square element had high convergence rates for non-distorted meshes. For distorted meshes, this element loses the global C^1 continuity, and the convergence rates deteriorated. This element can be applied with satisfactory accuracy to solve plate problems with non-distorted meshes. The accuracy deteriorates for distorted meshes.

The H_5 high-order quadrilateral and triangular elements also had high convergence rates for non-distorted meshes. The rates were smaller for distorted meshes for both elements but still with good accuracy. The H_5 high-order quadrilateral had higher rates than the triangular element. Both elements recovered the second-order derivatives of the transversal displacement, and the H_5 element had the same rates for distorted and non-distorted meshes. These elements can be applied with satisfactory accuracy and convergence rates to conforming approximation for problems which require C^1 continuity with distorted and non-distorted meshes.

We highlight the simpler implementation of the proposed bases because of the tensor-based nature compared with other plate elements in the literature. Another aspect is the exponential convergence rates for the examples considered and the use of distorted meshes. We have extended the presented bases for three-dimensional elements to be applied to Stokes flow problems, shell formulations and Cahn–Hilliard equation.

ACKNOWLEDGEMENTS

The authors would like to thank the Conselho Nacional de Desenvolvimento Científico e Tecnológico (CNPq) for the financial support of this work.

REFERENCES

1. Wang DW, Katz IN, Szabo BA. Implementation of C^1 triangular element based on p -version of the finite element method. *Computer & Structures* 1984; **19**:381–392.
2. Karniadakis GEM, Sherwin S. *Spectral/hp Element Method for Computational Fluid Dynamics* (2nd edn). Oxford University Press: Oxford, 2005.
3. Bittencourt ML. *Computational Solid Mechanics: Variational Formulation and High Order Approximation* (1st edn). CRC Press, 2014.
4. Chinosi C, Sacchi G, Scapolla T. A hierarchical family of conforming finite elements for the solution of plate bending problems. *Computer Methods in Applied Mechanics and Engineering* 1990; **80**:327–336.
5. Bittencourt ML. Fully tensorial nodal and modal shape functions for triangles and tetrahedra. *International Journal for Numerical Methods in Engineering* 2005; **63**:1530–1558.
6. Nguyen-xuan H, Rabczuk T, Bordas S, Debonnie JF. Superconvergent isogeometric free vibration analysis of Euler–Bernoulli beams and Kirchhoff plates with new higher order mass matrices. *Computer Methods in Applied Mechanics and Engineering* 2015; **286**:230–267.
7. Zienkiewicz OC, Taylor RL. *The Finite Element Method for Solid and Structural Mechanics* (6th edn), Vol. 2. Butterworth-Heinemann: Oxford, 2005.

8. Oñate E. *Structural Analysis with Finite Element Method: Linear Statics, Beam, Plates and Shells*, Vol. 2. Springer: Barcelona, 2013.
9. Venttsel E, Krauthammer T. *Thin Plates and Shells: Theory, Analysis and Applications*. Marce Dekker Inc: New York, 2001.
10. Okabe M. Full-explicit interpolation formulas for the Argyris triangle. *Computer Methods in Applied Mechanics and Engineering* 1993; **106**:381–394.
11. Touzot G, Dhatt G. *The Finite Element Method Displayed*. John Wiley and Sons: New York, 1985.
12. Bhatti MA. *Advanced Topics in Finite Element Analysis of Structures with Computations Using Mathematics and Matlab*. John Wiley & Sons: Hoboken, New Jersey, USA, 2006.
13. Bell K. Refined triangular plate bending finite element. *International Journal For Numerical Methods in Engineering* 1969; **1**:101–122.
14. Domínguez V, Sayas FJ. A simple Matlab implementation of the Argyris element. *ACM Transactions on Mathematical Software* 2008; **35**(2):1–11.
15. Peano A. Hierarchies of conforming finite elements for plane elasticity and plate bending. *Computers & Mathematics with Applications* 1976; **2**:211–224.
16. Bernadou M. C^1 -curved finite elements and applications to plate and shell problems. *Journal of Computational and Applied Mathematics* 1994; **50**:133–144.
17. Petera J, Pittman FT. Isoparametric Hermite elements. *International Journal For Numerical Methods in Engineering* 1994; **37**:3489–3519.
18. Šolín P, Segeth K. Hierarchic higher-order Hermite elements on hybrid triangular/quadrilateral meshes. *Mathematics and Computers in Simulation* 2007; **76**:198–204.
19. Papanicolopulos SA, Zervos A. A method for creating a class of triangular C^1 finite elements. *International Journal for Numerical Methods in Engineering* 2012; **89**:1437–1450.
20. Walkington NJ. A C^1 tetrahedral finite element without edge degrees of freedom. *Journal on Numerical Analysis* 2014; **52**:330–342.
21. Gopalacharyulu S. A higher order conforming rectangular plate element. *International Journal for Numerical Methods in Engineering* 1973; **6**:305–308.
22. Bardell NS. Free vibration analysis of a flat plate using the hierarchical finite element method. *Journal of Sound and Vibration* 1991; **151**:263–289.
23. Zhang S. On the full $C^1 - Q^k$ finite element spaces rectangle and cuboids. *Advanced in Applied Mathematics and Mechanics* 2010; **2**(6):701–721.
24. Ahmadi A, Surana KS, Maduri RK, Romkes A, Reddy JN. High order global differentiability local approximation for 2-D distorted quadrilateral elements. *International Journal for Computational Methods in Engineering Science and Mechanics* 2009; **10**:1–19.
25. Surana KS, Gupta P, Reddy JN. Galerkin and least-square finite element process for 2-D Helmholtz equation in h, p, k framework. *International Journal for Computational Methods in Engineering Science and Mechanics* 2007; **8**:341–361.
26. Nguyen-xuan H, Rabczuk T, Bordas S, Debonnie JF. A smoothed finite element method for plate analysis. *Computer Methods in Applied Mechanics and Engineering* 2008; **197**:11184–1203.
27. Miranville A. Sixth-order Cahn–Hilliard equations with singular nonlinear terms. *Applicable Analysis* 2015; **94**(10):2133–2146.
28. Schwab C. *p- and hp-Finite Element Methods: Theory and Applications in Solid and Fluid Mechanics*, Numerical mathematics and scientific computation. Oxford University Press: Oxford, 1998.
29. Szabó BA, Babuska I. *Finite Element Analysis*. Wiley: New York, 1991.